

A spectroscopic survey of Orion KL between 41.5 and 50 GHz

J. R. Rizzo¹, B. Tercero², and J. Cernicharo²

¹ Departamento de Astrofísica. Centro de Astrobiología (INTA-CSIC). Ctra. M-108, km. 4, E-28850 Torrejón de Ardoz, Spain
e-mail: ricardo.rizzo@cab.inta-csic.es

² Grupo de Astrofísica Molecular. Instituto de Ciencia de Materiales de Madrid (CSIC). Calle Sor Juana Inés de la Cruz 3, Cantoblanco, E-28049 Madrid, Spain

Received October 21, 2016; accepted May 20, 2017

ABSTRACT

Context. The nearby massive star-forming region Orion KL is one of the richest molecular reservoirs known in our Galaxy. The region hosts newly formed protostars, and the strong interaction between their radiation and their outflows with the environment results in a series of complex chemical processes leading to a high diversity of interstellar tracers. The region is therefore one of the most frequently observed sources, and the site where many molecular species have been discovered for the first time.

Aims. With the availability of powerful wideband backends, it is nowadays possible to complete spectral surveys in the entire mm-range to obtain a spectroscopically unbiased chemical picture of the region.

Methods. In this paper we present a sensitive spectral survey of Orion KL, made with one of the 34 m antennas of the Madrid Deep Space Communications Complex in Robledo de Chavela, Spain. The spectral range surveyed is from 41.5 to 50 GHz, with a frequency spacing of 180 kHz (equivalent to $\approx 1.2 \text{ km s}^{-1}$, depending on the exact frequency). The *rms* achieved ranges from 8 to 12 mK.

Results. The spectrum is dominated by the $J = 1 \rightarrow 0$ SiO maser lines and by radio recombination lines (RRLs), which were detected up to $\Delta n = 11$. Above a 3σ level, we identified 66 RRLs and 161 molecular lines corresponding to 39 isotopologues from 20 molecules; a total of 18 lines remain unidentified, two of them above a 5σ level. Results of radiative modelling of the detected molecular lines (excluding masers) are presented.

Conclusions. At this frequency range, this is the most sensitive survey and also the one with the widest band. Although some complex molecules like $\text{CH}_3\text{CH}_2\text{CN}$ and CH_2CHCN arise from the hot core, most of the detected molecules originate from the low temperature components in Orion KL.

Key words. Line: formation – Surveys – Stars: formation – ISM: clouds – ISM: molecules – Radio lines: ISM

1. Introduction

Orion KL has been widely recognized as the nearest high-mass star-forming region at a distance of 414–418 pc (Menten et al. 2007; Kim et al. 2008), and one of the richest molecular reservoirs known in the Galaxy.

It hosts newly formed protostars, with strong interaction between their radiation and their outflows with the environment. Diverse chemical processes are therefore favoured in the region, which results in a high variety of molecules detected. Indeed, this is the site where many molecular species have been discovered for the first time (e.g. methyl acetate, Tercero et al. 2013). After several observational works (e.g. Blake et al. 1987; Schilke et al. 2001; Tercero et al. 2010; Gong et al. 2015), at least four different molecular components have been identified in a relatively small volume. There are two compact sources, the *hot core*, characterized by high temperatures ($T_K \sim 100\text{--}300 \text{ K}$) and the *compact ridge*, with $T_K \sim 100\text{--}150 \text{ K}$. The third component is a quite extended *plateau* (with an angular size of up to $30''$), characterized by a warm molecular outflow at $T_K \sim 150 \text{ K}$. The hot core, the compact ridge and the outflow are immersed within the cooler ($T_K \sim 40\text{--}60 \text{ K}$) *extended ridge* or ambient cloud. These gas components could be resolved with single dish telescopes because they display different radial velocities and line widths. The Orion KL region is therefore an excellent testbed for the search of new molecules and also for the chemical characterization of those already known.

Many spectral line surveys have been carried out toward Orion KL covering a large range of frequencies (see Table 1 of Gong et al. 2015). In recent years, we can mention the IRAM 30m millimeter survey (Tercero et al. 2010), the Herschel/HIFI submillimeter and Far IR survey (Crockett et al. 2014), the submillimeter survey carried out with the Odin satellite (Olofsson et al. 2007; Persson et al. 2007), and the Effelsberg-100m telescope 1.3 cm survey (Gong et al. 2015).

However, the spectral range around 7 mm remains almost unexplored. At the best of our knowledge, the most complete survey up to date is that of Goddi et al. (2009a), which covers a frequency range optimized for the $J = 1 \rightarrow 0$ SiO maser emission lines (from 42.3 to 43.6 GHz).

Besides the SiO lines, the 40–50 GHz spectral window is potentially rich in several complex organic molecules, and hosts several transitions also identified at higher frequencies (3, 2, and 1 mm), but at lower energy levels. At these frequencies the presence of a wealth of radio recombination lines (RRLs) is also remarkable.

In this paper we present the results of a spectral survey in the Orion KL region, in the frequency range from 41.5 to 50 GHz (6 to 7.2 mm in wavelength). Sect. 2 describes the technical aspects of the survey, while Sect. 3 summarizes the results. A radiative model of the molecular emission is presented in Sect. 4, and the conclusions are enumerated in Sect. 5.

2. The spectral survey

We used the DSS-54 antenna, one of the 34m dishes available at the NASA's Madrid Deep Space Communications Complex (MDSCC), to perform a sensitive spectral survey of Orion KL. The observations were done in different runs from December 2013 to February 2014.

The survey was performed using a cooled high electron mobility transistor (HEMT) receiver (Rizzo & García-Miró 2013) and the two circular polarizations have been recorded. The receiver temperature remained around 40 K. The resulting system temperature varied from 90 to 190 K (in antenna temperature units), depending on the frequency, elevation and weather conditions. The backend was a new wideband backend (Rizzo et al. 2012), which provides 1.5 GHz of instantaneous bandwidth and a resolution of 180 kHz (equivalent to $\approx 1.2 \text{ km s}^{-1}$ at the observed frequencies), for each circular polarization.

The survey was conducted in position switching mode in six sub-bands, with a superposition of 100 MHz between two consecutive sub-bands, in order to check consistency and eliminate possible image sideband effects. Total integration time was 1490 minutes (on source). For each sub-band the integration time varied from 97 to 422 minutes, in order to reach to a uniform *rms* (1-sigma) level between 4 and 6 mK, on an antenna temperature scale.

Observations were carried out in winter nights, under good weather conditions. The atmospheric opacity has been measured during each observing session by means of tipping curves, and resulted to be between 0.07 and 0.11. During the observations, individual spectra have been corrected by atmospheric opacity and antenna gain due to elevation, obtaining the antenna corrected scale (T_a^*).

Data were processed using CLASS, a part of the GILDAS software¹. Spectra from different runs were averaged and baseline subtracted. The final spectrum was converted to main beam brightness temperature (T_{mb}) according to the usual expression

$$T_{\text{mb}} = T_a^* / \eta_{\text{mb}}, \quad (1)$$

where η_{mb} is the main beam efficiency (Wilson et al. 2009). The most relevant antenna parameters for different scale conversions, including density flux S , are summarized in Table 1. Unless otherwise specified, we use the T_{mb} scale throughout the paper.

3. Results

3.1. Overall emission

Figure 1 shows the resulting spectrum in the whole observed band. The upper panel displays the full range both in frequency and in intensity. We see that the spectrum is dominated by the emission of SiO masers and RRLs. Some well known molecules (CS, H_2CO , HC_3N , CH_3OH) are also intense and usually associated with both, cold and hot gas.

The middle panel depicts a zoom in intensity, where it is possible to distinguish a number of other, more complex molecules, particularly SO_2 , $\text{CH}_3\text{CH}_2\text{CN}$, HNCO , CH_3OCOH , and OCS . As shown in the model (Sect. 4), these molecules are associated with the hottest parts of the region.

The three lower panels are small spectral windows (indicated in green in the middle panel) which display the richness

of spectral lines and different line widths. We identified a total of 66 RRLs and 161 molecular lines above a 3σ level, of which 18 lines remain unidentified (U lines hereafter). The relative number of molecular lines with respect to RRLs is therefore $161/66 \approx 2.4$. This is ≈ 4 times higher than the ratio obtained at 1.3 cm (for example Gong et al. 2015, who detected 164 RRLs and 97 molecular lines), but notably lower than that found at millimeter wavelengths, where Tercero et al. (2010) identified more than 14400 molecular lines but only a few dozens of RRLs.

Therefore, the 7 mm band is especially useful in carrying out spectroscopic studies where the emission of RRLs and molecular lines are both of interest. Within some GHz of bandwidth, this band has a well balanced number of RRLs and molecular lines. At cm wavelengths, the number of molecular lines is quite low, while at mm wavelengths the high density of molecular lines and the large separation in frequency of the RRLs makes it difficult to simultaneously study the atomic ionised and the molecular components.

The procedure employed for line identification (such as smoothing, catalogues, and cross-check with other surveys) is outlined in Sect. 4.

3.2. Radio recombination lines

The detected 66 RRLs include 50, 12, and 4 lines corresponding to hydrogen, helium, and carbon, respectively. Hydrogen has been detected at a maximum Δn (the difference between principal quantum numbers of the upper and lower levels) of 11. All the detected lines can be well characterized by Gaussian fittings, whose parameters are indicated in Table 2. For each detection, the table contains the line name (ordered by increasing Δn), frequency, velocity-integrated line intensity, peak velocity, full width at half maximum, and peak temperature. One-sigma errors are displayed within parenthesis. Frequencies have been obtained from the MADCUBA_IJ package.²

Possible blending with molecular lines or other RRLs are indicated as notes in the last column of Table 2. In some cases (H64 β , H83 δ , and H107 κ) we could not separate the contribution of the blending lines, and the corresponding fitting has not been considered in subsequent analysis. The line H81 δ is clearly detected, but the spectrum is suffering from a series of unwanted features in specific channels ("spikes") at close frequencies; therefore, the fitting seriously underestimates the line intensity (probably up to a factor of 3).

For each atom, Fig. 2 depicts the distribution of velocities as a function of frequencies. The unweighted mean velocities of hydrogen and helium agree within uncertainties, with values of $-4.0 \pm 1.2 \text{ km s}^{-1}$ for hydrogen and $-3.6 \pm 1.8 \text{ km s}^{-1}$ for helium, while for the carbon lines we obtain $+9.3 \pm 1.9 \text{ km s}^{-1}$. To compute these values we included all the lines detected not affected by blending, and the error was estimated as the maximal individual error divided by the square root of the number of lines. The corresponding mean velocities weighted by the inverse square of the individual errors are -2.9 ± 0.1 , -3.0 ± 0.4 , and $+9.4 \pm 0.7 \text{ km s}^{-1}$ for hydrogen, helium and carbon, respectively. As expected, these values are dominated by the α lines which have the smallest uncertainties. The computed velocities are compatible with hydrogen and helium arising from the HII region M42, while the carbon recombination lines originate from the photon-dominated region (PDR) at the interface between M42 and the associated molecular cloud (the Orion Bar, see Cuadrado et al. 2015; Gong et al. 2015).

¹ GILDAS is a radio astronomy software developed by IRAM. See <http://www.iram.fr/IRAMFR/GILDAS/>.

² <http://cab.inta-csic.es/madcuba/>.

Based on their own data and other works, Goddi et al. (2009a) reported that RRL velocities increase with frequency, and explain this effect by the presence of a density gradient within the HII region. We decided to explore such hypothesis by a careful reading of the available bibliography. First, Goddi et al. (2009a) report “*velocities ranging from -5 to -10 km s $^{-1}$* ” based on three RRLs (H53 α , He53 α , and H76 γ), but they do not provide individual fitting; we measure a mean velocity of the H53 α line of -3.29 ± 0.04 km s $^{-1}$. Second, the other observations used for the hypothesis are those at 71–122 GHz from Turner (1991) (18 RRLs, including four α lines from hydrogen) and at 215–247 GHz from Sutton et al. (1985) (2 RRLs, only one α line from hydrogen). Turner (1991) reported a mean velocity of -3.4 km s $^{-1}$, but unfortunately did not provide individual fitting of the lines. Sutton et al. (1985) reported $+4$ km s $^{-1}$ for the H30 α line, but this is clearly contaminated by a rather strong line of $^{33}\text{SO}_2$ at ≈ 231.9003 GHz (Esplagues et al. 2013a).

After the work of Goddi et al. (2009a), several new surveys have been performed at different wavelengths. We therefore searched for the available information about α RRLs from hydrogen. Besides our own survey, we selected those works providing individual fitting (Sutton et al. 1985; Gong et al. 2015), or with the possibility to gather frequency calibrated data, as the IRAM 30m data provided by Tercero et al. (2010) and the GBT 4 mm survey of Frayer et al. (2015), available online³. The results are summarized in Table 3, and depicted in Fig. 3. Data include Gaussian fitting of α hydrogen RRL velocities from H30 α to H71 α , covering a wide range of frequencies from 17 to 232 GHz. We do not see in the figure or the table any significant variation of the velocities at any frequency, except the H30 α line, which is affected by blending, as already commented above. Therefore, we have not found any evidence for the claimed density gradient in the HII region.

Line widths are also quite uniform for each atom. We computed mean values of 21.9 ± 3.4 , 16.4 ± 6.2 , and 5.4 ± 3.4 km s $^{-1}$ for hydrogen, helium and carbon, respectively, which are in agreement with previous results (Gong et al. 2015).

In order to test the physical conditions of the HII region, we computed the ratio of peak temperatures for two hydrogen RRLs which lie at close frequencies. These ratios were then compared to the expected values under LTE conditions, following the procedure outlined by Brocklehurst & Seaton (1972). We excluded the ratios involving the H81 δ and H83 δ lines (see notes in Table 2). The result is depicted in the Fig. 4, where the measured ratios are plotted as a function of the LTE ratio. We see in this figure that the excitation of RRLs at these frequencies are close to LTE, within the uncertainties.

We also measured the helium abundance by computing the velocity-integrated line ratio between the same RRL from helium and hydrogen. We used all the available α , β , and γ lines, excluding H64 β due to blending. These ratios are a measure of the helium abundance under LTE conditions, assuming that all the helium is singly ionized and both Strömgren spheres are identical. The resulting value is 8.3 ± 1.2 %, which agrees with previous measurements in this source (Gong et al. 2015), and is close to Solar System values (Wilson & Rood 1994).

3.3. SiO emission

We detected a total of 5 lines from SiO, which are shown in Fig. 5. The lines correspond to the vibrational numbers $\nu = 0$, 1, and 2 of the main isotopologue, and to $\nu = 0$ of ^{29}SiO and

^{30}SiO . Overall, the line shapes agree with the single-dish results presented by Goddi et al. (2009a).

The most intense lines are masers corresponding to $\nu = 1$ and 2 of the main isotopologue. These lines are double-peaked and cover the velocity range from -16 to $+27$ km s $^{-1}$. Goddi et al. (2009b) have mapped these lines using the Very Large Array (VLA) and found that the emission arises from the inner part of the circumstellar structure associated with source I, with a maximum size of 100 AU.

The bright and very narrow feature in the $\nu = 2$ line at ≈ -1.4 km s $^{-1}$ is reported here for the first time. This component is not present in previous observations of Goddi et al. (2009a,b), obtained with even better spectral resolution. The lack of a similar feature in the $\nu = 1$ line may indicate that the emission of both maser lines arises from slightly different regions, as Goddi et al. (2009b) suggested.

The bulk of the $\nu = 0$ emission from ^{29}SiO and ^{30}SiO lines appears as a single component matching approximately the same velocity range as the $\nu = 1$ and 2 lines of ^{28}SiO . The high resolution maps (Goddi et al. 2009b) show that the emission of the four lines is confined to a distance of ≈ 100 AU to a young stellar object known as source I. Goddi et al. (2009b) also pointed out significant variations (at least two orders of magnitude) in the brightness temperature. The above facts and further modelling of radiative pumping allow the authors to conclude that the ^{29}SiO and ^{30}SiO $\nu = 0$ line emission is non thermal.

The line shape of the $\nu = 0$ line from ^{28}SiO is similar to those of ^{29}SiO and ^{30}SiO , although it has a broader spatial distribution (Goddi et al. 2009b), probably due to an outflow or a disc with a size of ≈ 600 AU in size, produced in the last 10^3 yr (Tercero et al. 2011; Niederhofer et al. 2012).

The emission of the ground vibrational state of ^{28}SiO has been observed at several rotational transitions up to $8 \rightarrow 7$ (e.g. Beuther et al. 2005; Tercero et al. 2011; Niederhofer et al. 2012). All these lines except $1 \rightarrow 0$ have Gaussian-like shapes and do not show hints of maser emission (in fact, Tercero et al. 2011, satisfactorily modelled their emission under thermal regimes). The shape of the $\nu = 0$ $J = 1 \rightarrow 0$ spectrum, as shown here, is rather different from the other $\nu = 0$ lines of ^{28}SiO and the thermal modelling of Tercero et al. (2011) is not able to reproduce the observed shape and intensity. Therefore it seems probable that the line is caused at least partially by maser emission, which has also been proposed by Chandler & de Pree (1995).

In addition to the main velocity component, the $\nu = 0$ lines of the three isotopologues have large wings from -40 to $+60$ km s $^{-1}$. The wings have been mapped in other rotational lines using interferometers: ($J = 1 \rightarrow 0$: Goddi et al. 2009b, VLA), ($J = 2 \rightarrow 1$: Plambeck et al. 2009, CARMA), and ($J = 5 \rightarrow 4$, $6 \rightarrow 5$: Zapata et al. 2012; Niederhofer et al. 2012, ALMA). All those high resolution observations show that this wide component arises from a bipolar outflow driven by source I (Goddi et al. 2009b).

4. Radiative model of the molecular emission

4.1. Overall description

Figure 6 displays the observed spectrum with more detail, after applying Hanning-smoothing of four contiguous channels, i.e., after degrading the spectral resolution to ~ 0.7 MHz. The intensity scale was in some cases zoomed to improve the visibility of weak lines (grey and yellow boxes of Fig. 6). Superimposed on the observed spectrum is also the result of the line identifica-

³ <http://vizier.cfa.harvard.edu/viz-bin/VizieR?-source=J01491662>

tion and further modelling. The SiO species and RRLs, although identified, are not part of the model.

The complete list of the identified species is presented in Table 4. The frequencies have been obtained from the CDMS⁴ (Müller et al. 2001, 2005), the JPL⁵ (Pickett et al. 1998), and private catalogues (J. Cernicharo, private communication). In all cases, we selected the frequency having the highest precision or that which provides the most complete information about hyperfine components. Most of the lines have been successfully identified, with only two U lines at a 5–6 σ level, at 46387.9 and 49765.7 GHz. The first U line has a width of $\approx 10 \text{ km s}^{-1}$, while the second one has $\approx 20 \text{ km s}^{-1}$. If confirmed, the 46387.9 GHz line may arise from the hot core and the other one from the plateau. Due to the low signal-to-noise ratio, it is hard to provide a robust characterization of the line shapes. All lines identified in this survey correspond to abundant molecules previously detected in this source (e.g. Blake et al. 1987; Sutton et al. 1995; Schilke et al. 2001; Goddi et al. 2009a; Tercero et al. 2010, 2011).

For many of the identified species, we previously derived physical parameters and column densities based on data from the IRAM line survey at 3, 2 and 1.3 mm (Tercero et al. 2010), which have been already published in a series of papers (see Table B3 of Cernicharo et al. 2016 for references). Due to the wide frequency range of that survey and the detailed analysis of the different components, we expect that the previous results for the modelled species are well constrained. Therefore, as a first approach we applied the models already performed to fit the lines of the IRAM 30m line survey to model the molecular emission at 7 mm.

We have built new radiative models for those molecules lacking previous modelling at this or other frequency bands after considering the differences attained from the use of different telescopes and frequencies. We fitted simultaneously both the cold and hot components in all the species. To do so, we used the MADEX code (Cernicharo 2012), which solves simultaneously the radiative transfer and the statistical equilibrium equations using local thermodynamic equilibrium (LTE); when the collisional rates were available, we proceeded with the large velocity gradient approach (LVG). A total of 5020 species from 1107 families⁶ can be modelled by this code.

We introduced the physical parameters of the different components found in the source (kinetic temperature T_K , H_2 volume density $n(H_2)$, source diameter d_{sou} , LSR velocity v_{LSR} , and line width Δv) according to either the typical values found in the literature and our previous Gaussian analysis of the lines. Furthermore, we also have taken into account the telescope dilution and the relative offsets between each cloud component with respect to the pointing position. We have chosen the column density of each cloud component as the free parameter. The nature of this method is iterative, which allowed us to introduce corrections to the original values of T_K and $n(H_2)$ in LVG calculations to improve the fitting. The discrepancies between the original and corrected values were below 20% in all cases.

At some frequencies, baseline fluctuations may produce differences in line intensity up to $\Delta T_{\text{mb}} \sim \pm 0.02 \text{ K}$. Therefore, the uncertainties may grow up to 20% for those lines having an observed intensity below $T_{\text{mb}} = 0.05 \text{ K}$.

We estimated the uncertainties of the resulting column densities supported by the analysis already done in the IRAM 30m survey (Tercero et al. 2010). There is not a remarkable new source of uncertainties in the new data presented in this work, especially for the molecules displaying a high signal-to-noise ratio in their lines. According to this analysis, the newly modelled molecules have uncertainties in the column density below 30%.

The physical parameters and the column densities obtained by the models are summarized in Table 6, where the contribution of every molecule to the different components is presented. Detailed results for each species are discussed in the next two subsections.

4.2. Agreement with models for the IRAM 30m survey

Most of the molecules with previous models have the bulk of their emission arising from the hot core. As described in the previous section, we used the physical parameters of those models as initial guesses.

We satisfactorily reproduced the emission of some of these species (HCS^+ , CCS, NH_2CHO , CH_3CH_2CN v_{13}/v_{21} , $^{34}SO_2$, $^{33}SO_2$, HC_3N $v_6=1$, and CH_2CHCN) without having to modify any parameters in the models (Tercero et al. 2010; Motiyenko et al. 2012; Daly et al. 2013; Esplugues et al. 2013a,b; López et al. 2014). A look at the Table 6 shows that these molecules have minor or absent contributions from the extended ridge and are therefore well described by the models at 1, 2, and 3 mm. In the case of NH_2CHO , the upper limit to the column density in this survey is well constrained by the model of Motiyenko et al. (2012).

Some other species (CH_3CH_2CN , SO_2 , $^{13}CH_3OH$, HC_3N , HC_5N , OCS, CS, C_3S , and HNCO) are more ubiquitous and have significant contribution from both the hot and the cold components. We have adapted the models of Daly et al. (2013) for CH_3CH_2CN , Esplugues et al. (2013a) for SO_2 , Kolesniková et al. (2014) for $^{13}CH_3OH$, Esplugues et al. (2013b) for HC_3N and HC_5N , Tercero et al. (2010) for OCS, CS, and C_3S , and Marcelino et al. (2009) for HNCO in order to properly fit the lines of these species. In all cases, it was necessary to modify the column densities of the cold components with respect to the previous models. For SO_2 , CH_3CH_2CN and $^{13}CH_3OH$ we had to reduce the column densities of the extended ridge by a factor of two.

The case of ^{13}CS is the most outstanding, whose column density has been reduced by up to a factor of ten in the cold component. This drastic change implies an intriguingly high $N(CS)/N(^{13}CS)$ ratio (from 100 to 250), which should be studied through future and more detailed observations and models.

For C_3S we introduced for the first time an extended ridge component, which is evident in the $J=8 \rightarrow 7$ line (with upper level energy around 10 K).

In the case of $C^{33}S$ we detected only a narrow line, compatible with the extended ridge, which is by far the major contributor to the line profile. The warm components remain at an intensity level below 0.05 K, corresponding to the upper limits quoted in Table 6.

In short, we noted that the 7 mm lines are more sensitive to small variations in the column densities of the cold component than lines at shorter wavelengths. This survey is, therefore, more adequate to constrain the contribution of the extended ridge gas.

Although all species discussed here have been previously detected in this source, some of them are only tentatively identified near the detection limit of our data: NH_2CHO , $O^{13}CS$, CCS, $^{33}SO_2$, CH_3CH_2CN v_{13}/v_{21} , and HC_3N $v_7=2$ (see Fig. 6). There-

⁴ <http://www.astro.uni-koeln.de/cgi-bin/cdmssearch>.

⁵ <http://spec.jpl.nasa.gov/ftp/pub/catalog/catform.html>.

⁶ We call family to a group of molecules containing all the isotopologues of a given species and all the vibrationally excited molecules, like for example SiO, ^{29}SiO , ^{30}SiO , and SiO $v = 1, 2, \dots$

fore, the derived column densities for these species have to be considered as upper limits.

4.3. New models

CH₃OH (methanol). A total of 10 lines of the main isotopologue of methanol are detected, equally distributed in A- and E-substates. Six of the lines are in the ground vibrational state, and four of them correspond to the first vibrationally excited state. The only maser is the $7_0 \rightarrow 6_1A^+$ transition, which is a well known class I maser in several Galactic sources, including Orion KL (e.g. Haschick et al. 1990). Orion KL was, in fact, the first source where a methanol maser line was detected (Barrett et al. 1971). The $7_0 \rightarrow 6_1A^+$ line shape (Haschick et al. 1990) is remarkably similar to the $8_0 \rightarrow 7_1A^+$ line (Ohishi et al. 1986), having a thermal component of $\approx 4 \text{ km s}^{-1}$ and a very narrow maser component with a width of only 0.22 km s^{-1} or less. Unfortunately, the spectral resolution of this survey prevents us to separate both components. Models of methanol in the ground state and in its first vibrationally excited state have been performed considering the same components as those used for $^{13}\text{CH}_3\text{OH}$. We note that the abundance ratio $[\text{CH}_3\text{OH}]/[^{13}\text{CH}_3\text{OH}]$ is between 5-15 for the different components. These values are far from the isotopic $^{12}\text{C}/^{13}\text{C}$ ratio of 45 derived by Tercero et al. (2010) in the source. Therefore, the lines from the main isotopologue of this abundant organic species are optically thick also at these frequencies. The derived column density for the hottest component (300 K) of A-CH₃OH $v_t=1$ is a factor 10 higher than that of the E-substate. Only one line of A-CH₃OH $v_t=1$ with $E_u=426 \text{ K}$ appears in this survey above the detection limit whereas the energies of the lines of the E-species are around $\sim 300 \text{ K}$ (see Table 4). Due to this difference in energy we obtain a different value for the column densities in the A- and E-substates. The low number of lines prevents a detailed analysis and we cannot accurately constrain the column densities.

H₂CO (formaldehyde). *ortho* and *para* formaldehyde have been modelled for all the lines between 7 mm and 1 mm. The *ortho*-to-*para* ratio is ~ 3 , as expected at high gas temperature. Only one line of o-H₂¹³CO with low intensity ($S_{ij} < 0.5$) is expected in the present frequency range, at 45.9 GHz. Because this line is only tentatively detected, the o-H₂¹³CO column density has to be considered as an upper limit.

CH₃OCOH (methyl formate). Ground state and vibrationally excited species ($v_t=0,1$) have been identified in the present data. For the model, we used the same components provided by Margulès et al. (2010). Lines corresponding to *b*-type transitions arising in the IRAM 30m data and the lines of the present survey have been fitted simultaneously. It is worth noting that the difference in the *a* and *b* dipole moments ($\mu_a = 1.63$ and $\mu_b = 0.68$ from Curl 1959) affects the opacity of the lines: many of the *a*-type transition-lines arising in the IRAM 30m survey are optically thick whereas those corresponding to *b*-type transitions are optically thin. By our procedure, we obtain a total column density of CH₃OCOH $v_t=0$ three times larger than the value provided by Margulès et al. (2010) and Carvajal et al. (2009), who assumed LTE conditions and optically thin emission. The first vibrationally excited state has been detected by means of several faint lines, most of them near the detection limit. We derived the column density by reducing the column density values obtained for the ground state to fit these lines in the present survey.

CH₃OCH₃ (dimethyl ether). We modelled this molecule by assuming that it is spatially correlated with methyl formate (Brouillet et al. 2013; Tercero et al. 2015). We initially fitted the four components described in Sect. 1. Although two of the

dimethyl ether lines have upper level energies as low as 2.3 K and 9.1 K, we had to remove the extended ridge to better reproduce the bulk of the dimethyl ether emission. The dominant component is by far the compact ridge, in agreement with high resolution observations (Brouillet et al. 2013).

NH₂D (deuterated ammonia). We used the four typical components of Orion KL (Sect. 1) to fit the NH₂D lines. We used the LTE approximation because only two lines are detected in our data. The intensity of the line at 49963 MHz results significantly overestimated, which suggests that the excitation of this species may be far from equilibrium.

CH₂OCH₂, CH₃COCH₃, CH₃NH₂ (ethylene oxide, acetone, methylamine). Most of the lines associated to these molecules (Table 4) are just tentatively detected (i.e. below the 3σ level) in this survey, and the derived column densities must be seen only as upper limits (Table 6). We modelled these species by fitting the four components to the lines depicted in Table 4 and also to those clearly detected at 3, 2, and 1 mm (Tercero et al. 2010).

5. Conclusions

This is the most complete spectral survey of Orion KL at the almost unexplored range from 6 to 7 mm wavelength. The sensitivity attained over the whole frequency range (approximately 15 mJy) allowed for the identification of 161 spectral lines from 21 molecular species and 66 RRLs from hydrogen, helium, and carbon. The total number of isotopologues detected in the survey grows up to 43, including the main species. Eight vibrationally excited species were also detected.

The spectrum of Orion KL at 7 mm is dominated by maser emission from SiO, ²⁹SiO, and ³⁰SiO, which are mainly consistent with previous observations. In addition, we report the detection of a new intense feature at -1.4 km s^{-1} in the $v=2$ SiO line.

The large number of RRLs, up to $\Delta n = 11$ is also remarkable. Velocities and line widths of the RRLs are consistent with those found at lower and higher frequencies, and the RRL emission is close to LTE. We have not found evidences for a previously reported change of RRL velocities with frequency, which has been claimed as the signpost of a density gradient within the H_{II} region.

The molecular spectrum has been modelled by computing the emission of all the detected molecules but SiO (due to maser emission). The approach for the model is based on results previously gathered in similar surveys at 1, 2, and 3 mm. This is the first radiative modelling of Orion KL for eight of the detected molecules, three of them with only upper limits for the column densities.

The results and further modelling demonstrates that the Q-band (6 to 8 mm wavelength) is especially sensitive to the low-temperature components in the environment of Orion KL. Some complex organic molecules, such as CH₃CH₂CN and CH₂CHCN, seem to mostly arise from the hot core; CH₃NH₂, is probably in the same group, but is only observed at the detection limit in the present work. Moreover, although CH₃OCH₃ has been detected through lines at very low upper energy levels, the extended ridge component is not required to properly fit the observed line profiles. We also note the lack of a cold contribution to the emission of NH₂CHO and CH₃COCH₃, molecules well detected in the IRAM 30m survey. The model of warm components used to fit their lines at 3, 2, and 1.3 mm properly constrains the emission of these species below the detection limit of the present work. Most of the remaining molecules seem to arise from both, the coldest and hottest parts of the source. A total

of 18 spectral lines remain unidentified, two of them at a level above 5-sigma.

Acknowledgements. This work was done under the Host Country Radio Astronomy program at MDSCC. The authors wish to thank the MDSCC staff (especially the radio astronomy engineer) for their kind and professional support during the observations. This work is supported by MICINN (Spain) grants CSD2009-00038, and AYA2012-32032. J.R.R. acknowledges the support from project ESP2015-65597-C4-1-R (MINECO/FEDER). B.T. and J.C. also thank MINECO grants CTQ 2013-40717 P and CTQ 2010-19008, and the ERC for synergy grant ERC-2013-Syg-610256-NANOCOSMOS.

References

- Barrett, A. H., Schwartz, P. R., & Waters, J. W. 1971, *ApJ*, 168, L101
 Beuther, H., Zhang, Q., Greenhill, L. J., et al. 2005, *ApJ*, 632, 355
 Blake, G. A., Sutton, E. C., Masson, C. R., & Phillips, T. G. 1987, *ApJ*, 315, 621
 Brocklehurst, M., & Seaton, M. J. 1972, *MNRAS*, 157, 179
 Brouillet, N., Despois, D., Baudry, A., et al. 2013, *A&A*, 550, 46
 Carvajal, M., Margulès, L., Tercero, B., et al. 2009, *A&A*, 500, 1109
 Cernicharo, J. 2012, *EAS Publications Series*, 58, 251
 Cernicharo, J., Kisiel, Z., Tercero, B., et al. 2016, *A&A*, 587, L4
 Chandler, C. J., & de Pree, C. G. 1995, *ApJ*, 455, L67
 Corey, G. C. 1984, *J. Chem. Phys.*, 81, 2678
 Corey, G. C. & McCourt, F. R. 1983, *J. Phys. Chem.*, 87, 2723
 Crockett, N. R., Bergin, E. A., Neill, J. L., et al. 2014, *ApJ*, 787, 112
 Cuadrado, S., Goicoechea, J. R., Pilleri, P. et al. 2015, *A&A*, 575, 82
 Curl, R. F. 1959, *J. Chem. Phys.*, 30, 1529
 Daly, A. M., Bermúdez, C., López, A., et al. 2013, *ApJ*, 768, 81
 Deguchi, S., Uyemura, M. 1984, *ApJ*, 285, D153
 Esplugues, G. B., Tercero, B., Cernicharo, J., et al. 2013a, *A&A*, 556, A143
 Esplugues, G. B., Cernicharo, J., Viti, S., et al. 2013b, *A&A*, 559, A51
 Frayer, D. T., Maddalena, R. J., Meijer, M., et al. 2015, *AJ*, 150, 39
 Goddi, C., Greenhill, L. J., Humphreys, E. M. L., et al. 2009a, *ApJ*, 691, 1254
 Goddi, C., Greenhill, L. J., Chandler, C. J., et al. 2009b, *ApJ*, 698, 1165
 Gong, Y., Henkel, C., Thorwirth, S., et al. 2015, *A&A*, 581, A48
 Green, S. & Chapman, S. 1978, *ApJS*, 37, 169
 Haschick, A. D., Menten, K. M., & Baan, W. A. 1990, *ApJ*, 354, 556
 Kim, M. K., Hirota, T., Honma, M., et al. 2008, *PASJ*, 60, 991
 Kolesníková, L., Tercero, B., Cernicharo, J., et al. 2014, *ApJ*, 784, L7
 Lique, F. & Spielfiedel, A. 2007, *A&A*, 462, 1179
 López, A., Tercero, B., Kisiel, Z., et al. 2014, *A&A*, 572, A44
 Marcelino, N., Cernicharo, J., Tercero, B., Roueff, E. 2009, *ApJ*, 690, L27
 Margulès, L., Huet, T. R., Demaison, J., et al. 2010 *ApJ*, 714, 1120
 Menten, K. M., Reid, M. J., Forbrich, J., & Brunthaler, A. 2007, *A&A*, 474, 515
 Monteiro, T. 1984, *MNRAS*, 210, 1
 Motiyenko, R. A., Tercero, B., Cernicharo, J., & Margulès, L. 2012, *A&A*, 548, A71
 Müller, H. S. P., Schlöder, F., Stutzki, J., & Winnewisser, G. 2005, *Journal of Molecular Structure*, 742, 215
 Müller, H. S. P., Thorwirth, S., Roth, D. A., & Winnewisser, G. 2001, *A&A*, 370, L49
 Niederhofer, F., Humphreys, E. M. L., & Goddi, C. 2012, *A&A*, 548, A69
 Ohishi, M., Kaifu, N., Suzuki, H., & Morimoto, M. 1986, *Ap&SS*, 118, 405
 Olofsson, A. O. H., Persson, C. M., Koning, N., et al. 2007, *A&A*, 476, 791
 Pickett, H. M., Poynter, R. L., Cohen, E. A., et al. 1998, *J. Quant. Spectr. Rad. Transf.*, 60, 883
 Plambeck, R. L., Wright, M. C. H., Friedel, D. N., et al. 2009, *ApJ*, 704, L25
 Persson, C. M., Olofsson, A. O. H., Koning, N., et al. 2007, *A&A*, 476, 807
 Rizzo, J. R., Pedreira, A., Gutiérrez Bustos, M., et al. 2012, *A&A*, 542, A63
 Rizzo, J. R., & García-Miró, G. 2013, *Highlights of Spanish Astrophysics VII*, 904
 Schilke, P., Benford, D. J., Hunter, T. R., Lis, D. C., & Phillips, T. G. 2001, *ApJS*, 132, 281
 Sutton, E. C., Peng, R., Danchi, W. C., et al. 1995, *ApJS*, 97, 455
 Sutton, E. C., Blake, G. A., Masson, C. R., & Phillips, T. G. 1985, *ApJS*, 58, 341
 Tercero, B., Cernicharo, J., López, A., et al. 2015, *A&A*, 582, L1
 Tercero, B., Cernicharo, J., Pardo, J. R., & Goicoechea, J. R. 2010, *A&A*, 517, A96
 Tercero, B., Kleiner, I., Cernicharo, J., et al. 2013, *ApJ*, 770, L13
 Tercero, B., Vincent, L., Cernicharo, J., Viti, S., & Marcelino, N. 2011, *A&A*, 528, A26
 Turner, B. E. 1991, *ApJS*, 76, 617
 Wernli, M., Wiesenfeld, L., Faure, A., & Valiron, P. 2007, *A&A*, 464, 1147
 Wilson, T. L., & Rood, R. 1994, *ARA&A*, 32, 191
 Wilson, T. L., Rohlfs, K., Hüttemeister, S. 2009, *Tools of Radio Astronomy*, (Springer-Verlag, Berlin)
 Zapata, L. A., Rodríguez, L. F., Schmid-Burgk, J., et al. 2012, *ApJ*, 754, L17

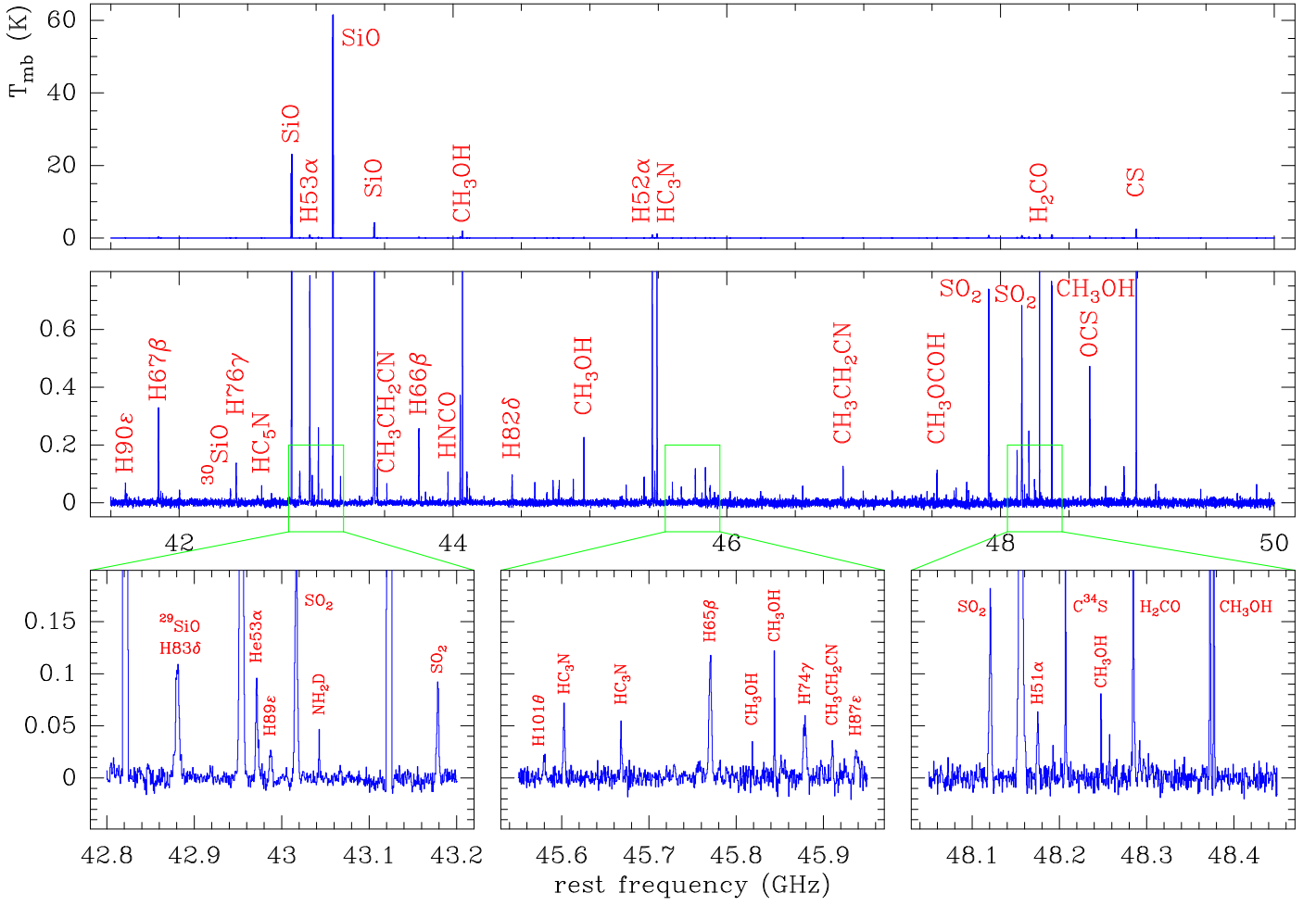


Fig. 1: Spectrum of Orion KL. Top panel: full range. Middle panel: zoom in intensity to see low intensity lines; green boxes are expanded in the three bottom panels, to show spectroscopic details. Some of the most intense lines are labelled.

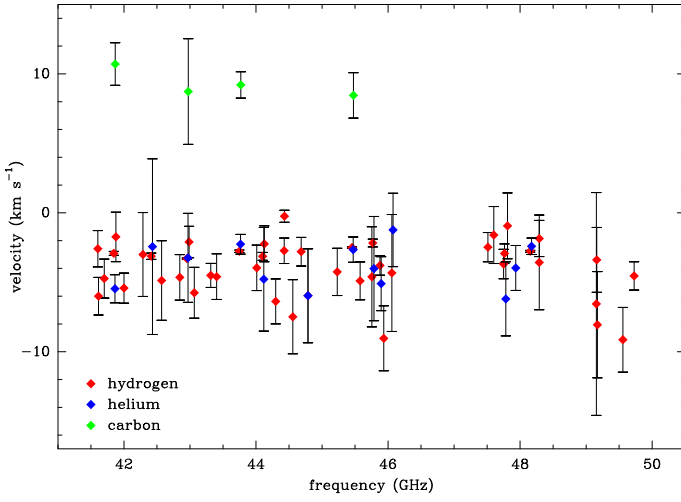


Fig. 2: Distribution of the velocities of the RRLs as a function of frequency. Atoms (hydrogen, helium, and carbon) are labelled in red, blue, and green, respectively.

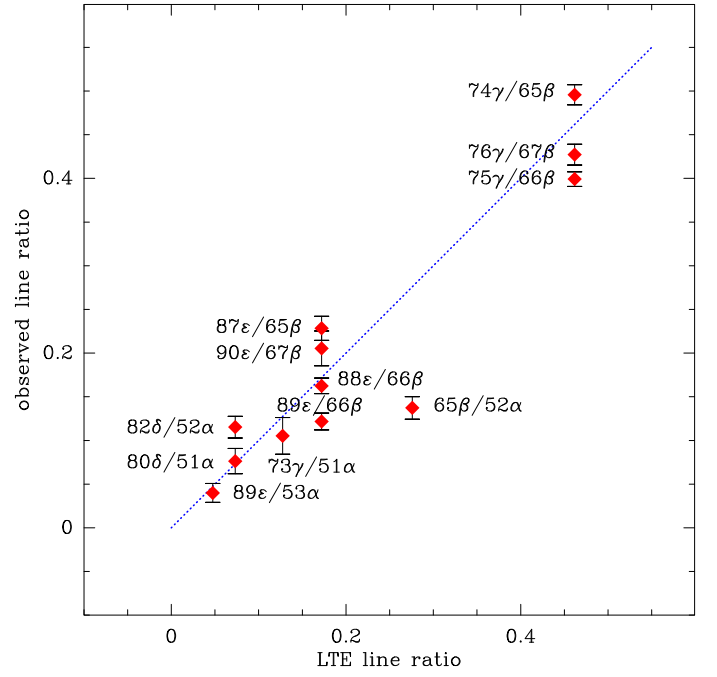


Fig. 4: Distribution of the measured line intensity ratios between pairs of hydrogen RRLs at nearby frequencies as a function of the predicted ratios under LTE conditions. The ratios are labelled and the bars represent 1.5-sigma errors. The dotted blue line corresponds to equal values between observed and predicted ratios under LTE conditions.

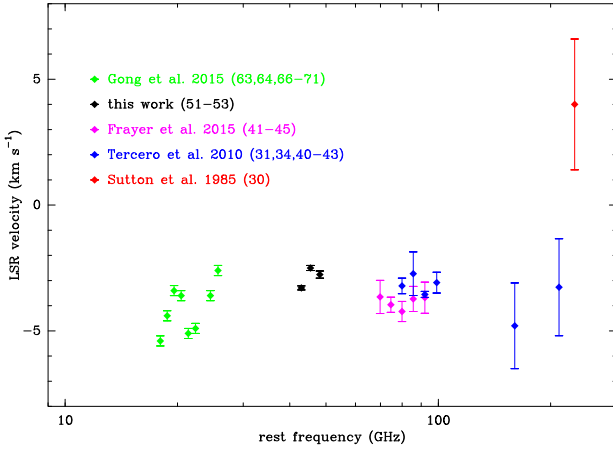


Fig. 3: LSR velocities of α RRLs from hydrogen in Orion KL, as a function of the frequency (on a logarithmic scale). Surveys used are indicated with different colours. Together with the references, the principal quantum numbers are indicated within parenthesis. Error bars correspond to 2-sigma values.

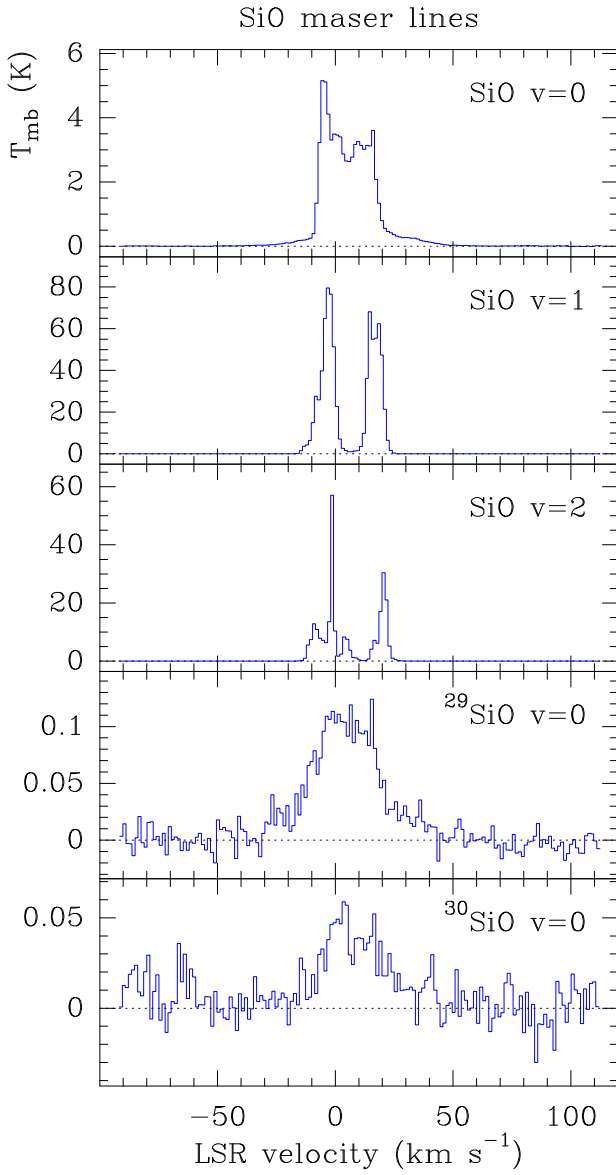


Fig. 5: The SiO $J = 1 \rightarrow 0$ lines detected in Orion KL. Isotopologues and vibrational numbers are indicated in each panel.

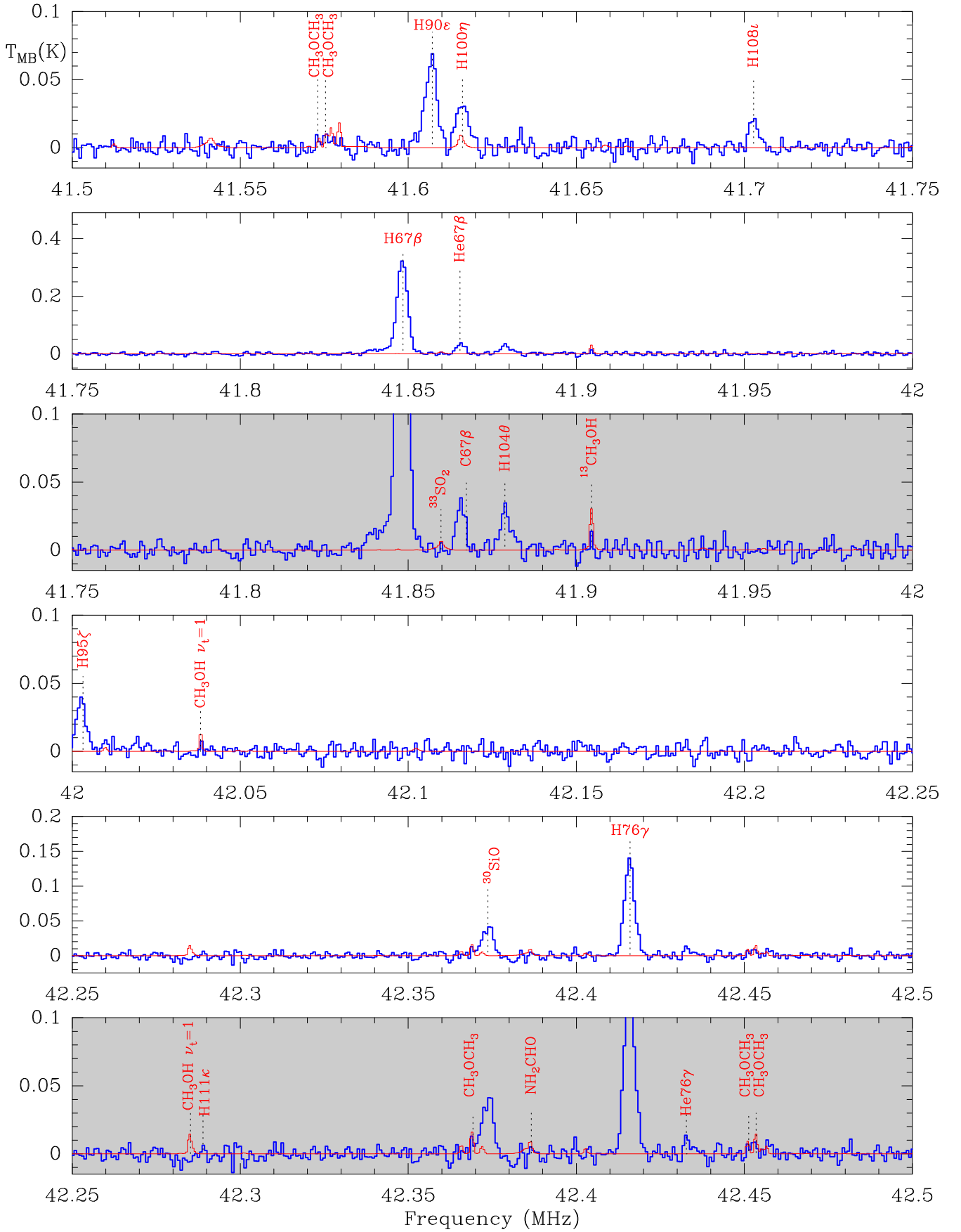


Fig. 6: Detailed view of the observed spectrum of Orion KL at 7 mm (in blue), superimposed to the identification of the most intense lines and the best fit model for the molecular species (in red). Each panel displays a width of approximately 250 MHz. In order to improve the visibility of low intensity lines, some frequency ranges are plotted with a zoom in intensity (grey boxes); a second level of zoom, when necessary, is also depicted (yellow boxes). To compute the rest frequencies, a velocity of $v_{\text{LSR}} = +9 \text{ km s}^{-1}$ is assumed. Note that the model results do not include the SiO masers nor the RRLs.

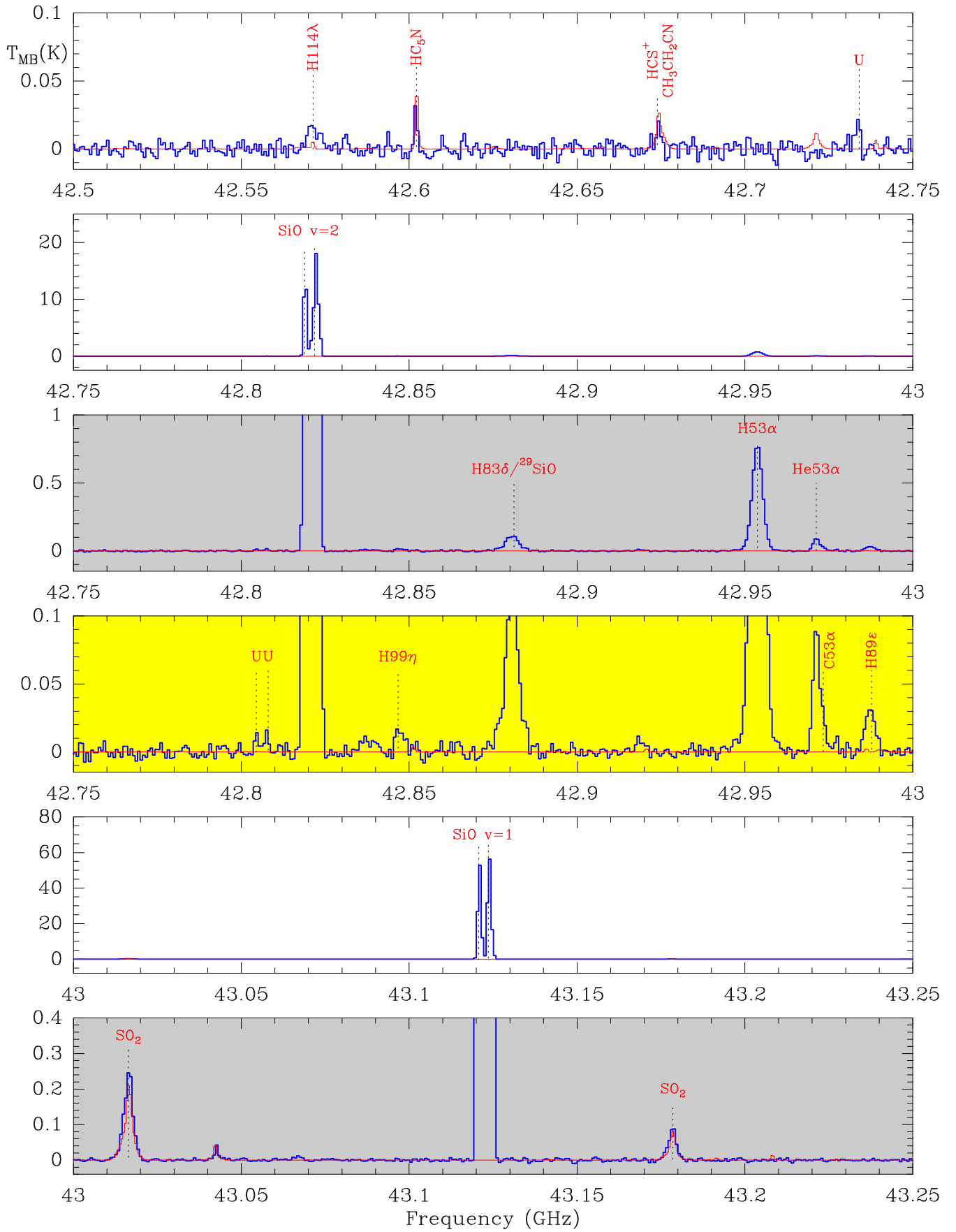


Figure 6: continued.

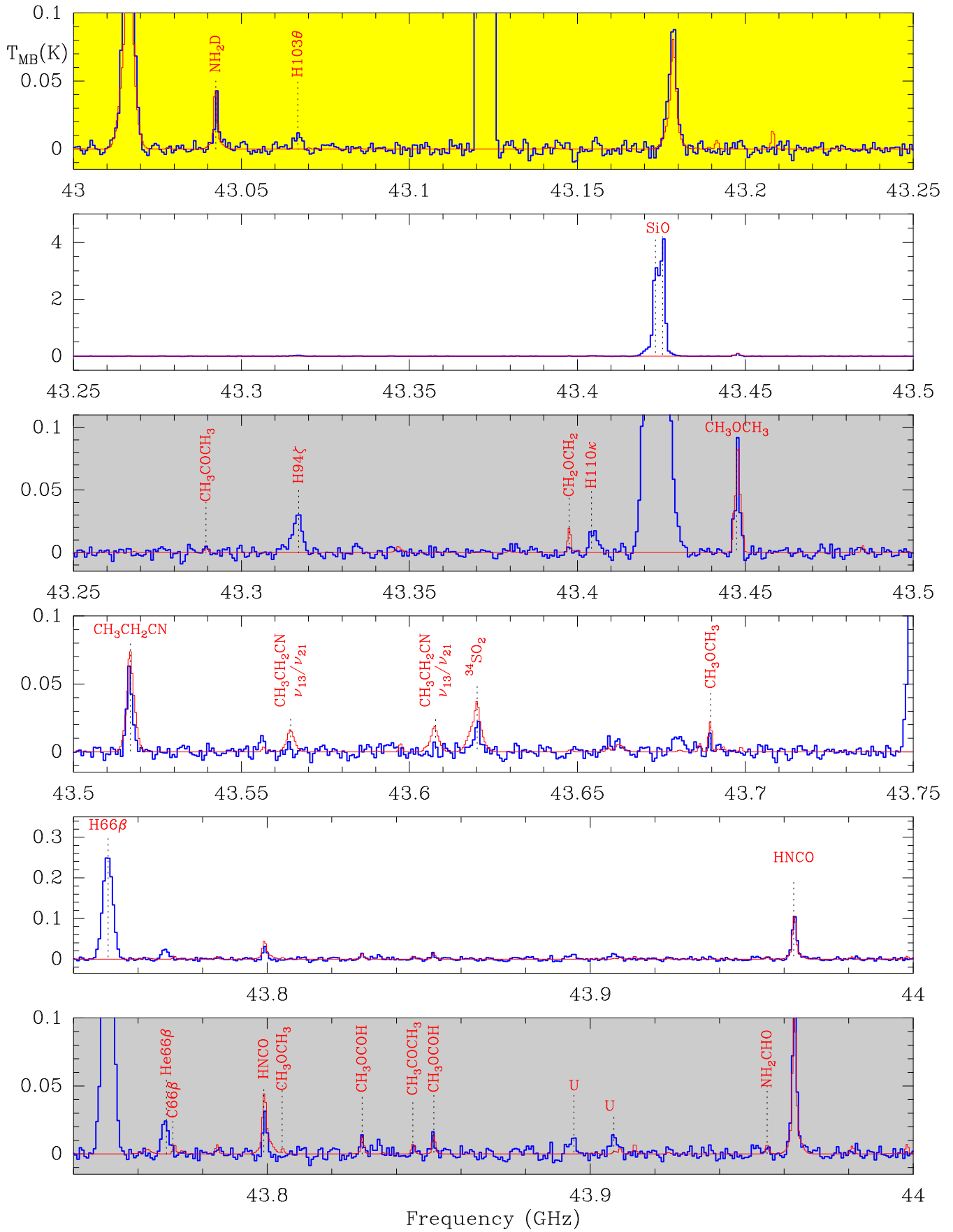


Figure 6: continued.

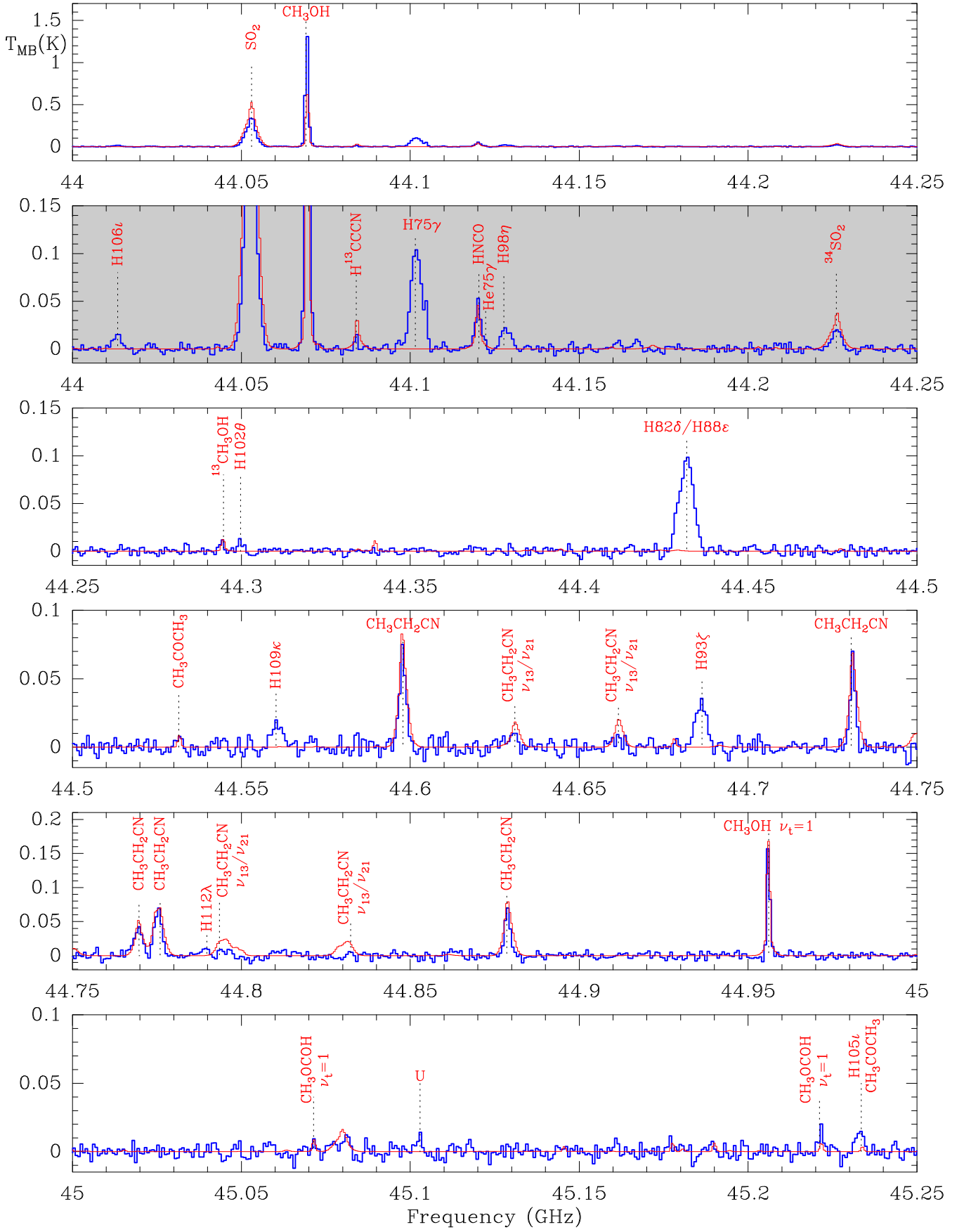


Figure 6: continued.

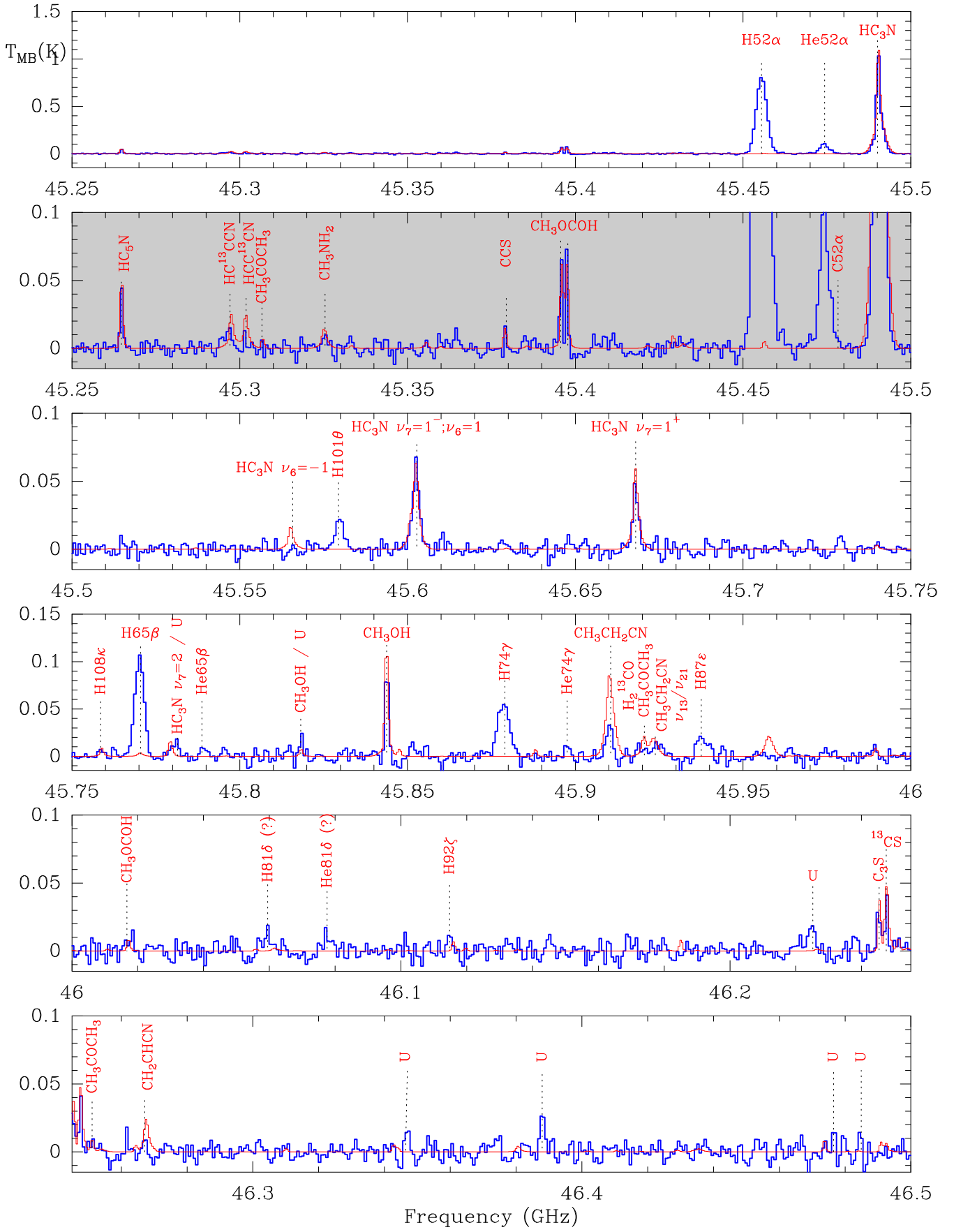


Figure 6: continued.

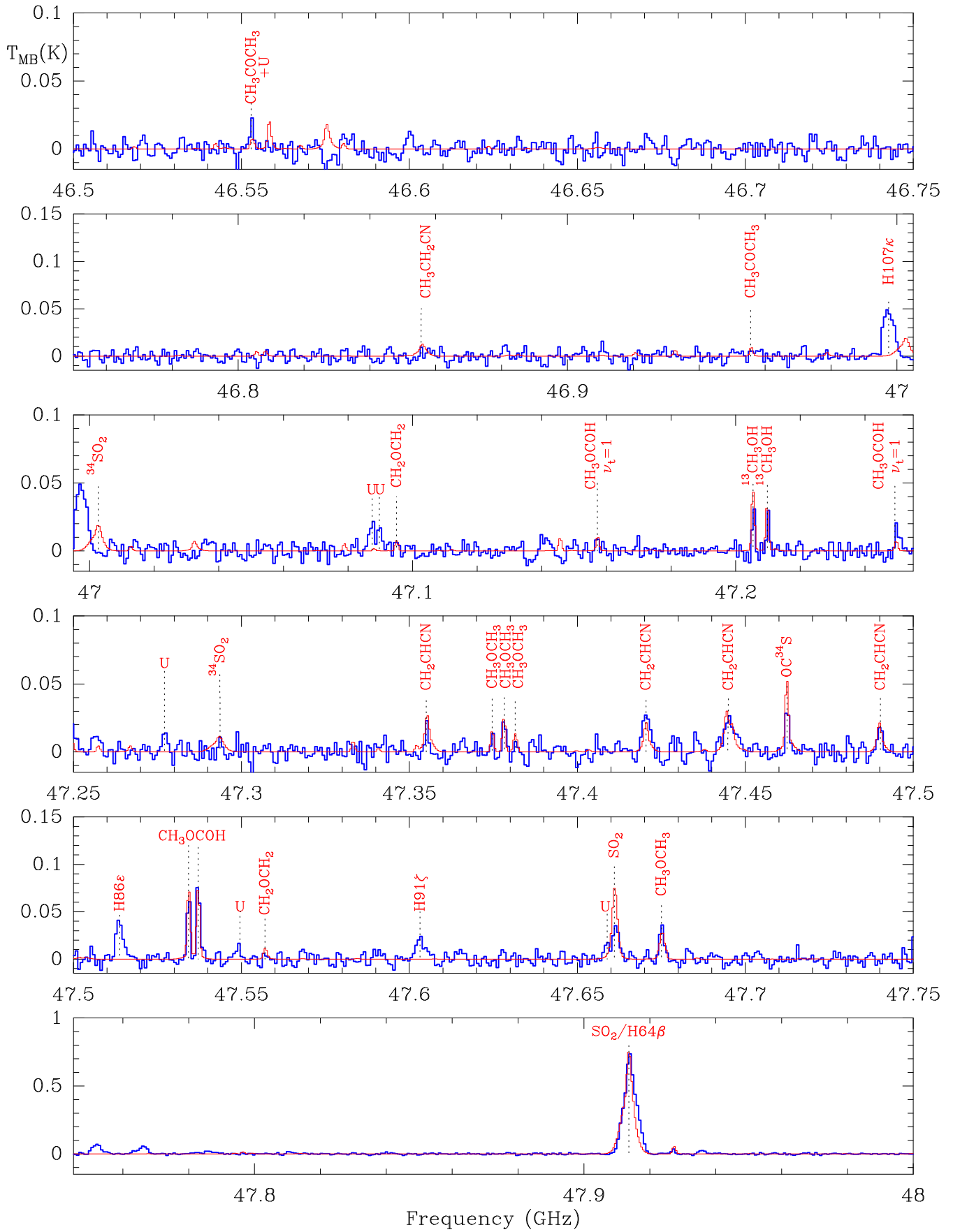


Figure 6: continued.

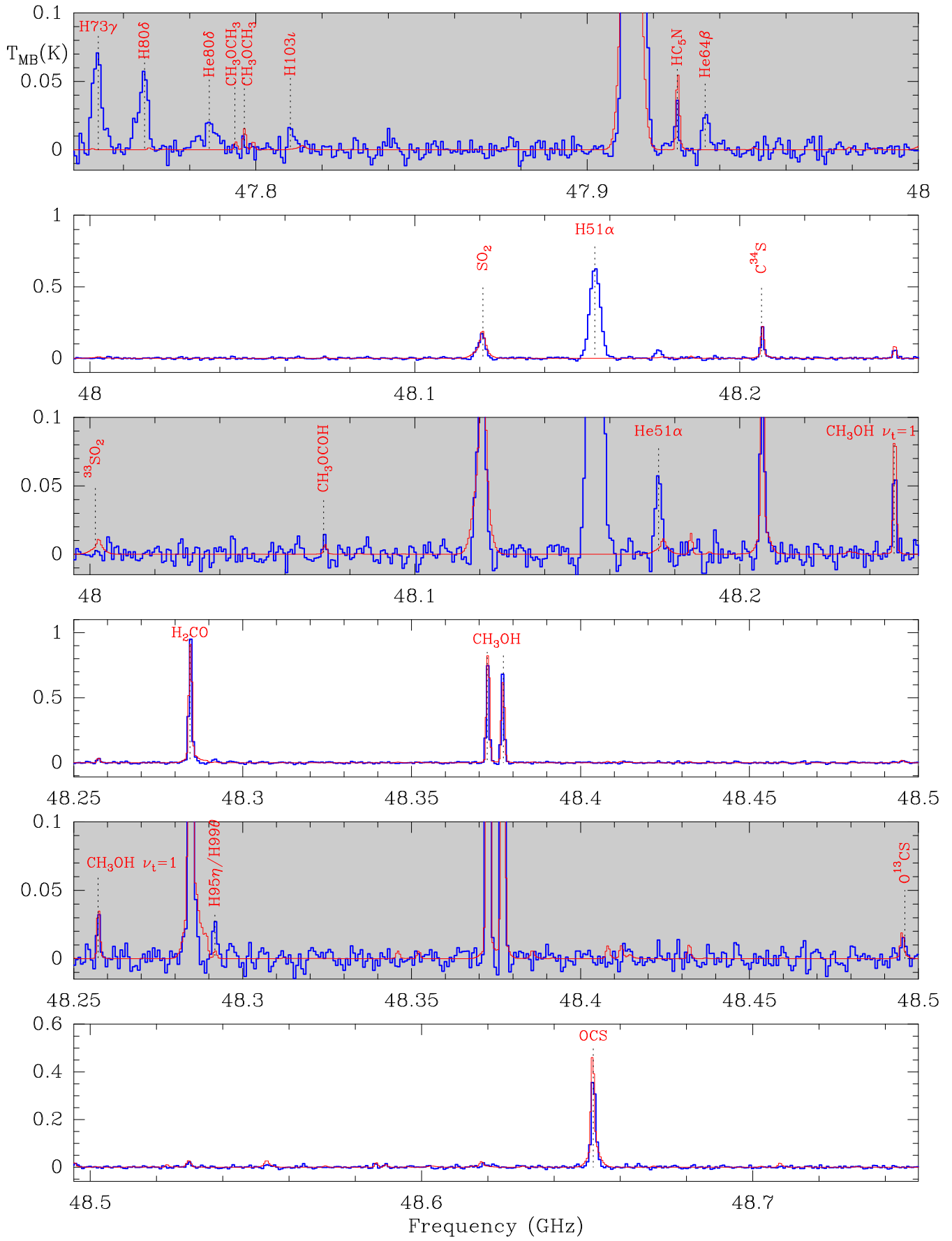


Figure 6: continued.

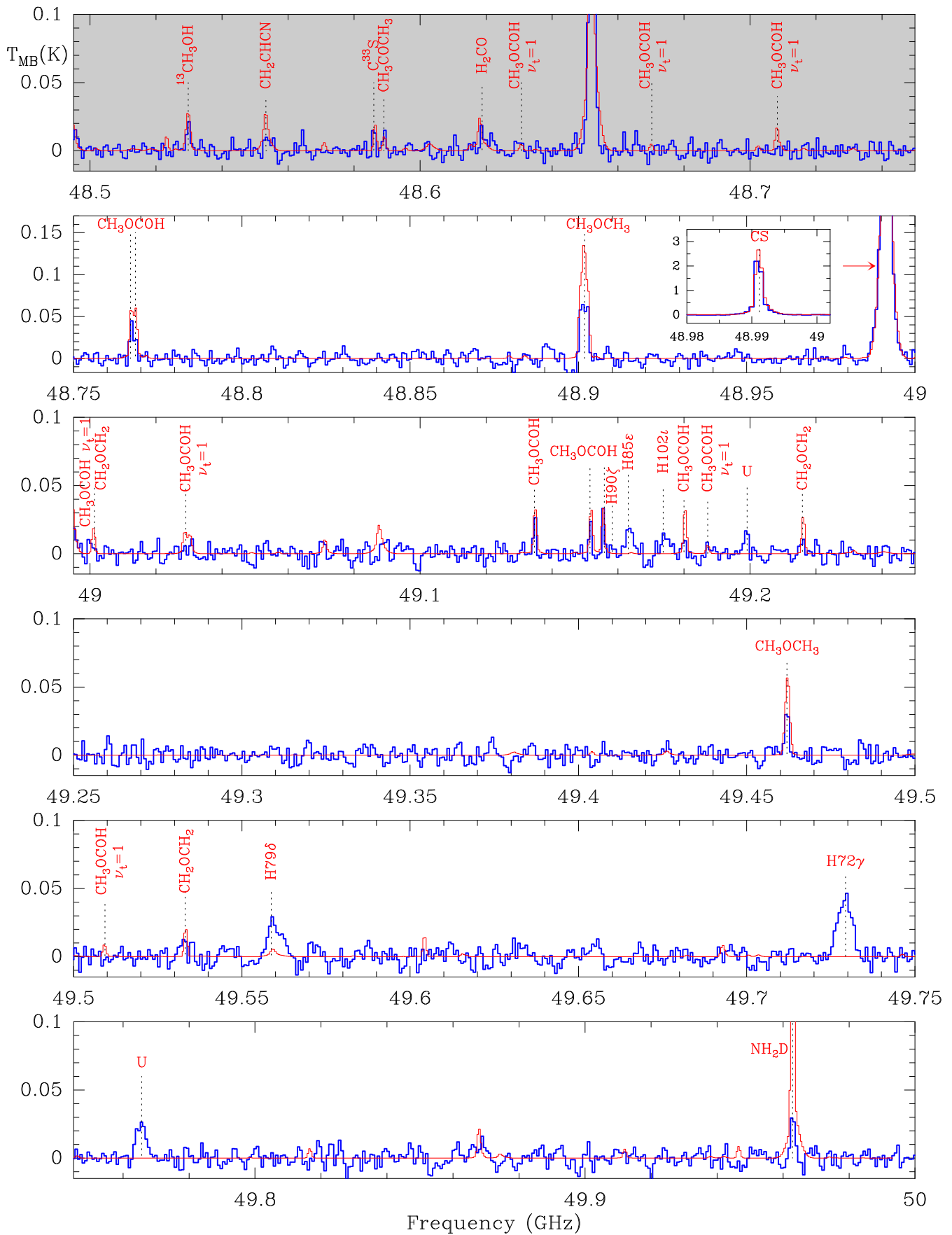


Figure 6: continued.

Table 1: DSS-54 antenna parameters

Parameter		value
Diameter	D	34 m
Beam size	$HPBW$	$2050''/\nu(\text{GHz})$
Aperture efficiency	η_A	0.46
Main beam efficiency	η_{mb}	0.52
Sensitivity	S/T_a^*	6.41 Jy/K

Table 2: Radio recombination lines detected

Line	Frequency MHz	Area K km s ⁻¹	Velocity km s ⁻¹	Width km s ⁻¹	Peak temperature K	Notes
$\Delta n = 1$						
H53 α	42951.9707	20.78 (0.07)	-3.29 (0.04)	24.82 (0.10)	0.787 (0.005)	
H52 α	45453.7217	20.97 (0.10)	-2.50 (0.05)	23.94 (0.13)	0.823 (0.007)	
H51 α	48153.6000	17.80 (0.10)	-2.76 (0.07)	24.24 (0.16)	0.690 (0.007)	
He53 α	42969.4730	1.57 (0.11)	-3.24 (3.20)	15.30 (3.89)	0.096 (0.007)	
He52 α	45472.2435	1.91 (0.34)	-2.65 (0.91)	16.92 (3.00)	0.106 (0.009)	
He51 α	48173.2220	0.97 (0.08)	-2.41 (0.60)	14.16 (1.37)	0.065 (0.008)	
C53 α	42973.3984	0.16 (0.11)	8.74 (3.80)	5.34 (4.20)	0.028 (0.008)	
C52 α	45476.3975	0.21 (0.33)	8.46 (1.63)	6.76 (3.50)	0.030 (0.009)	
$\Delta n = 2$						
H67 β	41846.5533	8.56 (0.10)	-2.92 (0.14)	24.85 (0.33)	0.323 (0.007)	
H66 β	43748.9539	6.47 (0.05)	-2.77 (0.09)	23.59 (0.21)	0.258 (0.004)	
H65 β	45768.4478	2.60 (0.07)	-2.17 (0.28)	21.57 (0.65)	0.113 (0.005)	
H64 β	47914.1849	20.41 (0.14)	9.96 (0.10)	28.47 (0.23)	0.674 (0.009)	(a)
He67 β	41863.6052	0.82 (0.09)	-5.47 (1.01)	19.84 (2.22)	0.039 (0.006)	
He66 β	43766.7811	0.37 (0.04)	-2.26 (0.71)	14.33 (1.66)	0.024 (0.054)	
He65 β	45787.0978	0.14 (0.06)	-4.01 (3.76)	13.61 (7.21)	0.010 (0.006)	
He64 β	47933.7093	0.33 (0.08)	-3.97 (1.62)	12.63 (3.76)	0.025 (0.008)	
C67 β	41867.4296	0.07 (0.08)	10.71 (1.53)	5.41 (4.11)	0.013 (0.006)	
C66 β	43770.7793	0.02 (0.02)	9.21 (0.95)	4.03 (2.07)	0.005 (0.004)	
$\Delta n = 3$						
H76 γ	42414.0908	3.57 (0.07)	-3.12 (0.22)	24.34 (0.54)	0.138 (0.005)	
H75 γ	44100.0954	2.99 (0.07)	-3.13 (0.28)	27.09 (0.68)	0.103 (0.004)	
H74 γ	45876.6701	1.55 (0.08)	-3.79 (0.69)	25.99 (1.50)	0.056 (0.006)	
H73 γ	47749.9800	1.88 (0.17)	-3.69 (1.06)	24.30 (2.81)	0.073 (0.012)	
H72 γ	49726.7007	1.10 (0.08)	-4.54 (1.02)	27.61 (2.16)	0.037 (0.006)	(b)
He76 γ	42431.3739	0.26 (0.14)	-2.43 (6.32)	15.56 (15.50)	0.016 (0.006)	
He75 γ	44118.0656	0.59 (0.41)	-4.68 (5.27)	19.08 (17.10)	0.029 (0.025)	(c)
He74 γ	45895.3643	0.15 (0.05)	-5.10 (1.95)	11.52 (3.26)	0.012 (0.005)	
$\Delta n = 4$						
H83 δ	42879.8047	3.87 (0.09)	3.44 (0.35)	33.00 (0.89)	0.110 (0.005)	(d)
H82 δ	44430.7088	2.65 (0.04)	-0.24 (0.43)	26.19 (0.40)	0.095 (0.005)	(e)
H81 δ	46057.3309	0.44 (0.11)	-4.33 (4.21)	30.43 (10.30)	0.014 (0.006)	(f)
H80 δ	47764.3497	0.97 (0.08)	-2.93 (0.69)	17.20 (1.73)	0.053 (0.007)	
H79 δ	49556.7953	0.71 (0.11)	-9.13 (2.33)	28.05 (4.54)	0.024 (0.008)	
He81 δ	46076.0986	0.41 (0.08)	-1.23 (2.65)	27.29 (6.18)	0.014 (0.005)	
He80 δ	47783.8130	0.27 (0.10)	-6.19 (2.67)	16.62 (9.40)	0.015 (0.007)	
$\Delta n = 5$						
H90 ϵ	41605.2445	2.14 (0.20)	-2.59 (1.31)	30.37 (3.36)	0.066 (0.012)	
H89 ϵ	42985.6946	0.79 (0.01)	-2.10 (1.13)	23.56 (2.55)	0.031 (0.005)	(g)
H88 ϵ	44427.9131	1.03 (0.06)	-2.73 (0.92)	23.15 (0.95)	0.042 (0.005)	(h)
H87 ϵ	45935.3946	0.86 (0.12)	-9.03 (2.34)	31.18 (5.53)	0.026 (0.008)	
H86 ϵ	47511.8739	0.56 (0.09)	-2.47 (1.06)	13.34 (2.28)	0.039 (0.009)	
H85 ϵ	49161.3453	0.30 (0.10)	-3.38 (2.33)	14.78 (5.48)	0.020 (0.009)	
$\Delta n = 6$						
H95 ζ	42000.6430	0.80 (0.09)	-5.41 (1.08)	20.75 (2.56)	0.036 (0.006)	
H94 ζ	43314.7537	0.72 (0.06)	-4.50 (0.87)	22.12 (2.13)	0.031 (0.004)	
H93 ζ	44684.2804	0.95 (0.08)	-2.79 (1.03)	25.88 (2.28)	0.035 (0.005)	
H91 ζ	47601.5859	0.41 (0.09)	-1.60 (2.05)	19.07 (4.86)	0.020 (0.007)	
H90 ζ	49155.8585	0.12 (0.15)	-6.56 (8.02)	11.03 (14.50)	0.010 (0.017)	(i)
$\Delta n = 7$						

Table 2: continued.

Line	Frequency MHz	Area K km s ⁻¹	Velocity km s ⁻¹	Width km s ⁻¹	Peak temperature K	Notes
H100 η	41613.9945	1.17 (0.10)	-6.00 (1.35)	32.52 (2.97)	0.034 (0.006)	(j)
H99 η	42845.8100	0.67 (0.07)	-4.64 (1.64)	28.80 (3.59)	0.022 (0.005)	
H98 η	44126.7461	0.49 (0.06)	-2.23 (1.29)	22.07 (2.55)	0.021 (0.004)	
H97 η	45459.2772	0.28 (0.08)	-3.32 (3.34)	22.46 (5.89)	0.012 (0.006)	(k)
H95 η	48289.7868	0.28 (0.58)	-3.57 (3.41)	8.35 (3.41)	0.031 (0.011)	
$\Delta n = 8$						
H104 θ	41877.3884	0.60 (0.11)	-1.73 (1.78)	21.28 (5.16)	0.027 (0.007)	
H103 θ	43064.7499	0.20 (0.04)	-5.75 (1.83)	18.01 (3.40)	0.010 (0.003)	
H102 θ	44297.4483	0.26 (0.06)	-6.38 (1.62)	15.92 (4.84)	0.015 (0.004)	
H101 θ	45577.6694	0.38 (0.06)	-4.90 (1.37)	16.76 (3.43)	0.021 (0.005)	
H99 θ	48290.0704	0.26 (0.08)	-1.85 (1.31)	7.99 (2.95)	0.031 (0.010)	
$\Delta n = 9$						
H108 ι	41700.7983	0.59 (0.07)	-4.73 (1.40)	23.37 (3.53)	0.024 (0.005)	
H106 ι	44011.4774	0.46 (0.06)	-3.96 (1.64)	25.13 (4.29)	0.017 (0.004)	
H105 ι	45231.0739	0.41 (0.07)	-4.25 (1.70)	19.22 (3.92)	0.020 (0.006)	(l)
H103 ι	47808.9329	0.16 (0.06)	-0.94 (2.37)	9.79 (3.71)	0.015 (0.007)	
H102 ι	49171.6054	0.29 (0.10)	-8.06 (3.82)	20.70 (8.41)	0.013 (0.009)	
$\Delta n = 10$						
H111 κ	42287.2908	0.11 (0.05)	-3.00 (3.02)	11.24 (5.23)	0.009 (0.006)	
H110 κ	43402.8801	0.29 (0.05)	-4.60 (1.64)	16.91 (3.09)	0.016 (0.005)	
H109 κ	44558.0836	0.38 (0.08)	-7.48 (2.67)	22.97 (5.14)	0.015 (0.006)	
H108 κ	45754.6765	0.38 (0.09)	-4.61 (3.60)	29.54 (3.60)	0.012 (0.025)	(m)
H107 κ	46994.5305	1.12 (0.08)	-9.45 (0.79)	22.24 (1.66)	0.047 (0.006)	(n)
$\Delta n = 11$						
H114 λ	42569.5866	0.47 (0.08)	-4.87 (2.86)	29.11 (5.89)	0.015 (0.005)	
H112 λ	44787.0910	0.20 (0.76)	-5.97 (3.38)	16.90 (6.71)	0.011 (0.007)	

Notes. (a) Blend with SO₂ (47913.600 MHz). 2-components fitting impossible. (b) Probably contaminated by H98 θ . (c) Blend with HNCO (44120.324 MHz). Separated. (d) Blend with ²⁹SiO maser. 2-components fitting impossible. (e) Blend with H88 ϵ . Separated. (f) Line clearly detected, but fitting not reliable due to spikes at close frequencies. (g) Contaminated by CH₃COCH₃ (42985.958 MHz). (h) Blend with H82 δ . Separated. (i) Close to CH₃OCOH doublet and H85 ϵ . (j) Probably contaminated by CH₃NH₂ (41615.387 MHz). (k) Very close to H52 α . Tentative fitting. (l) Probably contaminated by CH₃COCH₃ (45233.497 MHz). (m) Blend with CH₃CH₂CN (45758.528 MHz). Separated. (n) Blend with HNCS (46997.506 MHz). 2-components fitting impossible.

Table 3: LSR velocities of H α RRLs in Orion KL

Line	Frequency (GHz)	V_{LSR} (km s ⁻¹)	Error	Ref.
H30 α	231.9013	+4.0	1.3	1
H34 α	160.2115	-4.80	0.85	2
H31 α	210.5018	-3.27	0.96	2
H43 α	79.9127	-3.21	0.16	2
H42 α	85.6884	-2.73	0.43	2
H41 α	92.0344	-3.55	0.06	2
H40 α	99.0230	-3.08	0.21	2
H71 α	17.9926	-5.4	0.1	3
H70 α	18.7692	-4.4	0.1	3
H69 α	19.5911	-3.4	0.1	3
H68 α	20.4618	-3.6	0.1	3
H67 α	21.3844	-5.1	0.1	3
H66 α	22.3642	-4.9	0.1	3
H64 α	24.5099	-3.6	0.1	3
H63 α	25.6863	-2.6	0.1	3
H45 α	69.8296	-3.65	0.33	4
H44 α	74.6446	-3.96	0.15	4
H43 α	79.9127	-4.23	0.20	4
H42 α	85.6884	-3.73	0.25	4
H41 α	92.0344	-3.68	0.31	4
H53 α	42.9520	-3.29	0.04	5
H52 α	45.4537	-2.50	0.05	5
H51 α	48.1536	-2.76	0.07	5

References. (1) Sutton et al. (1985); (2) Tercero et al. (2010); (3); Gong et al. (2015) (4) Frayer et al. (2015); (5) this work.

Table 4: Line list

Observed Freq. (MHz)	Species	Rest Freq. (MHz)	Transition J_{K_a,K_c}	E_{upp} (K)	A_{ul} $\times 10^{-6}$ (s $^{-1}$)
41573.1	AA-CH ₃ OCH ₃	41573.290	19 _{5,14} -18 _{6,13}	208.3	0.07
41575.3	EE-CH ₃ OCH ₃	41575.465	19 _{5,14} -18 _{6,13}	208.3	0.06
41607.1	H90 ϵ	41605.242			
41616.2	H100 η	41613.994			
	CH ₃ NH ₂	41615.387	15 _{1,4} -15 _{0,5}	256.9	0.86
41702.7	H108 ι	41700.798			
41848.5	H67 β	41846.551			
41859.7	³³ SO ₂	41859.643	6 _{2,4} - 7 _{1,7}	29.0	0.14
41865.4	He67 β	41863.603			
41867.2	C67 β	41867.430			
41878.8	H104 θ	41877.388			
41904.6	A- ¹³ CH ₃ OH	41904.330	8 _{2,7} - 9 _{1,8}	119.3	0.31
42003.2	H95 ζ	42000.640			
42038.2	A-CH ₃ OH $v_t=1$	42038.245	22 _{9,1} -22 _{8,-1}	1268.9	0.09
42285.2	E-CH ₃ OH $v_t=1$	42284.886	$J_K=19_{-3}-18_{-2}$	762.1	0.09
42288.9	H111 κ	42287.291			
42369.3	EE-CH ₃ OCH ₃	42368.723	13 _{3,11} -12 _{4,8}	95.6	0.07
42372.9	³⁰ SiO	42373.424	$J=1-0$	2.0	2.83
42374.5	³⁰ SiO	42373.424	$J=1-0$	2.0	2.83
42386.6	NH ₂ CHO	42386.062	2 _{0,2} - 1 _{0,1}	3.1	4.64
42416.0	H76 γ	42414.088			
42432.7	He76 γ	42431.374			
42451.3	AA-CH ₃ OCH ₃	42450.801	16 _{4,13} -15 _{5,10}	146.5	0.07
42453.5	EE-CH ₃ OCH ₃	42453.197	16 _{4,13} -15 _{5,10}	146.5	0.07
42571.4	H114 λ	42569.587			
42602.2	HC ₅ N	42602.153	$J=16-15$	17.4	8.18
42673.9	HCS ⁺	42674.195	$J=1-0$	2.0	1.16
42675.3	CH ₃ CH ₂ CN	42674.211	11 _{1,10} -11 _{0,11}	30.2	0.47
42734.0	U				
42804.5	U				
42808.0	U				
42818.9	SiO $v=2$	42820.586	$J=1-0$	3523.4	3.00
42821.8	SiO $v=2$	42820.586	$J=1-0$	3523.4	3.00
42846.7	H99 η	42845.810			
42881.2	H83 δ	42879.802			
	²⁹ SiO	42879.947	$J=1-0$	2.1	2.94
42953.7	H53 α	42951.968			
42971.2	He53 α	42969.471			
42973.3	C53 α	42973.396			
42987.7	H89 ϵ	42985.692			
43016.4	SO ₂	43016.275	19 _{2,18} -18 _{3,15}	182.6	0.12
43042.4	NH ₂ D	43042.276	3 _{1,3} - 3 _{0,3} $v=1-0$	94.5	1.34
43066.8	H103 θ	43064.750			
43120.7	SiO $v=1$	43122.073	$J=1-0$	1771.3	3.02
43123.6	SiO $v=1$	43122.073	$J=1-0$	1771.3	3.02
43178.6	SO ₂	43178.167	23 _{2,22} -22 _{3,19}	259.9	0.08
43289.5	AA-CH ₃ COCH ₃	43289.395	13 _{10,3} -13 _{9,4}	77.8	2.10
43317.0	H94 ζ	43314.754			
43397.6	O-CH ₂ OCH ₂	43397.471	8 _{6,2} - 8 _{5,3}	78.3	1.25
43404.2	H110 κ	43402.880			
43423.2	SiO	43423.852	$J=1-0$	2.1	3.05
43425.3	SiO	43423.852	$J=1-0$	2.1	3.05
43447.4	AE-CH ₃ OCH ₃	43446.471	6 _{1,5} - 6 _{0,6}	21.1	0.51
	EA-CH ₃ OCH ₃	43446.471	6 _{1,5} - 6 _{0,6}	21.1	0.51
	EE-CH ₃ OCH ₃	43447.541	6 _{1,5} - 6 _{0,6}	21.1	0.51
	AA-CH ₃ OCH ₃	43448.612	6 _{1,5} - 6 _{0,6}	21.1	0.51
43517.0	CH ₃ CH ₂ CN	43516.196	5 _{1,5} - 4 _{1,4}	7.4	6.20
43564.6	CH ₃ CH ₂ CN v_{13}/v_{21}	43563.724	5 _{1,5} - 4 _{1,4} $v=3-3$	313.5	11.1
	CH ₃ CH ₂ CN v_{13}/v_{21}	43563.927	5 _{1,4} - 4 _{1,3} $v=5-5$	313.5	11.1

Table 4: continued.

Observed Freq. (MHz)	Species	Rest Freq. (MHz)	Transition J_{K_a,K_c}	E_{upp} (K)	A_{ul} $\times 10^{-6}$ (s $^{-1}$)
43607.8	CH ₃ CH ₂ CN v_{13}/v_{21}	43606.667	5 _{1,5} - 4 _{1,4} $\nu=0-0$	304.4	11.3
	CH ₃ CH ₂ CN v_{13}/v_{21}	43606.681	5 _{1,4} - 4 _{1,3} $\nu=2-2$	304.4	11.3
43620.1	³⁴ SO ₂	43619.944	9 _{3,7} -10 _{2,8}	62.6	0.19
43689.7	EE-CH ₃ OCH ₃	43689.344	16 _{4,12} -15 _{5,11}	146.5	0.08
43750.7	H66 β	43748.951			
43768.8	He66 β	43766.779			
	C66 β	43770.779			
43798.9	HNCO	43799.014	2 _{1,2} - 1 _{1,1}	46.4	0.74
43829.4	E-CH ₃ OCOH	43829.202	9 _{-2,7} - 9 _{-1,8}	29.6	0.17
43845.0	EE-CH ₃ COCH ₃	43844.921	18 _{11,7} -18 _{10,8}	139.3	2.95
43851.6	A-CH ₃ OCOH	43851.298	9 _{2,7} - 9 _{1,8}	30.2	0.17
43894.9	U				
43907.3	U				
43954.7	NH ₂ CHO	43954.458	2 _{1,1} - 1 _{1,0}	6.1	3.88
43963.0	HNCO	43963.039	2 _{0,2} - 1 _{0,1}	3.2	1.02
44013.4	H106 ι	44011.477			
44053.0	SO ₂	44052.873	6 _{2,4} - 7 _{1,7}	29.2	0.16
44069.1	A-CH ₃ OH	44069.367	7 _{0,1} - 6 _{1,1}	65.0	0.20
44084.0	H ¹³ CCCN	44084.162	$J=5-4$	6.3	0.63
44101.5	H75 γ	44100.093			
44120.3	HNCO	44119.876	2 _{1,1} - 1 _{1,0}	46.5	0.76
	He75 γ	44118.066			
44127.7	H98 η	44126.746			
44226.1	³⁴ SO ₂	44226.222	10 _{3,7} -11 _{2,10}	71.9	0.19
44294.7	E- ¹³ CH ₃ OH	44294.420	10 _{-1,10} - 9 _{-2,8}	122.2	0.12
44299.8	H102 θ	44297.448			
44431.8	H82 δ	44430.706			
	H88 ϵ	44427.913			
44531.5	EE-CH ₃ COCH ₃	44531.376	14 _{8,6} -14 _{7,7}	84.7	2.62
44560.2	H109 κ	44558.084			
44597.8	CH ₃ CH ₂ CN	44596.990	5 _{0,5} - 4 _{0,4}	6.4	6.95
44631.0	CH ₃ CH ₂ CN v_{13}/v_{21}	44630.164	5 _{0,5} - 4 _{0,4} $\nu=3-3$	312.5	12.5
	CH ₃ CH ₂ CN v_{13}/v_{21}	44630.426	5 _{0,5} - 4 _{0,4} $\nu=5-5$	312.5	12.5
44661.6	CH ₃ CH ₂ CN v_{13}/v_{21}	44660.925	5 _{0,5} - 4 _{0,4} $\nu=2-2$	303.5	12.6
	CH ₃ CH ₂ CN v_{13}/v_{21}	44660.940	5 _{0,5} - 4 _{0,4} $\nu=0-0$	303.5	12.6
44686.3	H93 ζ	44684.278			
44730.5	CH ₃ CH ₂ CN	44730.269	5 _{2,4} - 4 _{2,3}	10.9	5.90
44769.7	CH ₃ CH ₂ CN	44768.914	5 _{4,2} - 4 _{4,1}	24.2	2.53
	CH ₃ CH ₂ CN	44768.918	5 _{4,1} - 4 _{4,0}	24.2	2.53
44776.0	CH ₃ CH ₂ CN	44775.379	5 _{3,2} - 4 _{3,1}	16.5	4.51
44789.8	H112 λ	44787.091			
44793.5	CH ₃ CH ₂ CN v_{13}/v_{21}	44792.650	5 _{1,5} - 4 _{1,4} $\nu=1-1$	307.6	10.6
	CH ₃ CH ₂ CN v_{13}/v_{21}	44792.678	5 _{2,4} - 4 _{2,3} $\nu=0-0$	307.6	10.6
	CH ₃ CH ₂ CN v_{13}/v_{21}	44794.103	5 _{3,3} - 4 _{3,2} $\nu=3-3$	323.4	7.88
	CH ₃ CH ₂ CN v_{13}/v_{21}	44794.847	5 _{3,3} - 4 _{3,2} $\nu=4-4$	323.4	7.88
	CH ₃ CH ₂ CN v_{13}/v_{21}	44795.002	5 _{3,2} - 4 _{3,1} $\nu=5-5$	323.4	7.88
	CH ₃ CH ₂ CN v_{13}/v_{21}	44795.284	5 _{3,2} - 4 _{3,1} $\nu=3-3$	323.4	7.88
44832.3	CH ₃ CH ₂ CN v_{13}/v_{21}	44830.148	5 _{3,3} - 4 _{3,2} $\nu=1-1$	312.8	7.64
	CH ₃ CH ₂ CN v_{13}/v_{21}	44830.257	5 _{3,2} - 4 _{3,1} $\nu=0-0$	312.8	7.99
	CH ₃ CH ₂ CN v_{13}/v_{21}	44831.290	5 _{4,2} - 4 _{4,1} $\nu=1-1$	320.0	4.44
	CH ₃ CH ₂ CN v_{13}/v_{21}	44831.336	5 _{4,1} - 4 _{4,0} $\nu=2-2$	320.0	4.44
	CH ₃ CH ₂ CN v_{13}/v_{21}	44831.357	5 _{4,2} - 4 _{4,1} $\nu=0-0$	320.0	4.23
	CH ₃ CH ₂ CN v_{13}/v_{21}	44831.365	5 _{4,1} - 4 _{4,0} $\nu=0-0$	320.0	4.23
44878.6	CH ₃ CH ₂ CN	44878.102	5 _{2,3} - 2 _{2,2}	10.9	5.95
44956.1	E-CH ₃ OH $\nu_t=1$	44955.794	$J_K=2_0-3_1$	307.5	0.38
45071.4	A-CH ₃ OCOH $\nu_t=1$	45071.299	4 _{1,4} - 3 _{1,3}	194.5	1.17
45102.9	U				
45221.1	E-CH ₃ OCOH $\nu_t=1$	45221.427	4 _{1,4} - 3 _{1,3}	193.7	1.19
45233.5	H105 ι	45231.074			

Table 4: continued.

Observed Freq. (MHz)	Species	Rest Freq. (MHz)	Transition J_{K_a,K_c}	E_{upp} (K)	A_{ul} $\times 10^{-6}$ (s $^{-1}$)
	EE-CH ₃ COCH ₃	45233.560	$3_{2,2} - 2_{1,1}$	4.5	2.20
45264.7	HC ₅ N	45264.720	$J=17-16$	19.6	9.83
45297.1	HC ¹³ CCN	45297.335	$J=5-4$	6.5	6.85
45301.9	HCC ¹³ CN	45301.707	$J=5-4$	6.5	6.85
45306.6	EE-CH ₃ COCH ₃	45306.662	$9_{4,5} - 9_{3,6}$	34.6	2.03
45325.4	CH ₃ NH ₂	45324.879	$14_{1,4} - 14_{0,5}$	225.4	1.08
45379.5	CCS	45379.027	$N_J=3_4 - 2_3$	5.4	3.91
45395.6	E-CH ₃ OCOH	45395.802	$4_{1,4} - 3_{1,3}$	5.5	1.20
45397.8	A-CH ₃ OCOH	45397.360	$4_{1,4} - 3_{1,3}$	6.1	1.20
45455.5	H52 α	45453.719			
45474.3	He52 α	45472.241			
45478.3	C52 α	45476.395			
45490.1	HC ₃ N	45490.311	$J=5-4$	6.5	6.94
45565.8	HC ₃ N $v_6=1$	45564.962	$J_L=5_{-1} - 4_{-1}$	724.3	4.80
45579.4	H101 θ	45577.669			
45602.8	HC ₃ N $v_7=1$	45602.171	$J_L=5_{-1} - 4_{-1}$	326.6	6.67
	HC ₃ N $v_6=1$	45600.785	$J_L=5_1 - 4_1$	724.3	4.80
45668.0	HC ₃ N $v_7=1$	45667.549	$J_L=5_1 - 4_1$	326.6	6.70
45758.5	H108 κ	45754.676			
45770.4	H65 β	45768.445			
45781.5	HC ₃ N $v_7=2$	45778.894	$J_L=5_{-2} - 4_{-2}$	652.5	5.88
	HC ₃ N $v_7=2$	45779.070	$J_L=5_0 - 4_0$	649.3	7.00
	HC ₃ N $v_7=2$	45779.197	$J_L=5_2 - 4_2$	652.5	5.88
	U				
45788.8	He65 β	45787.095			
45818.2	A-CH ₃ OH	45818.114	$10_{1,-1} - 10_{1,1}$	143.3	0.008
	U				
45843.8	E-CH ₃ OH	45843.554	$J_K=9_3 - 10_2$	144.3	0.16
45879.0	H74 γ	45876.667			
45897.6	He74 γ	45895.364			
45910.5	CH ₃ CH ₂ CN	45909.515	$5_{1,4} - 4_{1,3}$	7.7	7.28
45920.6	EE-CH ₃ COCH ₃	45920.479	$12_{9,4} - 12_{8,5}$	65.9	2.32
	α -H ₂ ¹³ CO	45920.058	$4_{1,3} - 4_{1,4}$	31.9	0.31
45923.8	CH ₃ CH ₂ CN v_{13}/v_{21}	45922.352	$5_{1,4} - 4_{1,3} \nu=3-3$	313.8	13.0
	CH ₃ CH ₂ CN v_{13}/v_{21}	45922.766	$5_{1,5} - 4_{1,4} \nu=4-4$	313.8	13.0
45937.5	H87 ϵ	45935.392			
46016.7	A-CH ₃ OCOH	46017.032	$7_{1,6} - 7_{0,7}$	17.9	0.11
46059.5	H81 δ	46057.331			
46077.5	He81 δ	46076.099			
46115.6	H92 ζ	46112.177			
46225.2	U				
46245.3	C ₃ S	46245.623	$J=8-7$	10.0	0.74
46247.5	¹³ CS	46247.563	$J=1-0$	2.2	1.47
46251.1	EE-CH ₃ COCH ₃	46251.002	$11_{7,5} - 11_{6,6}$	53.1	2.56
46267.1	CH ₂ CHCN	46266.935	$5_{1,5} - 4_{1,4}$	8.8	7.34
46346.9	U				
46387.9	U				
46476.5	U				
46484.9	U				
46552.9	EE-CH ₃ COCH ₃	46552.825	$8_{3,5} - 8_{2,6}$	26.7	1.88
	U				
46855.5	CH ₃ CH ₂ CN	46855.211	$12_{1,11} - 12_{0,12}$	35.4	0.58
46955.6	EE-CH ₃ COCH ₃	46955.561	$12_{8,5} - 12_{7,6}$	63.7	2.79
46997.5	H107 κ	46994.530			
47002.7	³⁴ SO ₂	47002.372	$21_{3,19} - 20_{4,16}$	233.5	0.23
47087.5	U				
47089.7	U				
47095.0	p-CH ₂ OCH ₂	47094.971	$4_{4,1} - 4_{3,2}$	21.5	0.75
47157.2	A-CH ₃ OCOH $v_t=1$	47157.098	$4_{0,4} - 3_{0,3}$	194.1	1.42

Table 4: continued.

Observed Freq. (MHz)	Species	Rest Freq. (MHz)	Transition J_{K_a,K_c}	E_{upp} (K)	A_{ul} $\times 10^{-6}$ (s $^{-1}$)
47205.4	A- $^{13}\text{CH}_3\text{OH}$	47205.210	$1_{0,1}-0_{0,0}$	2.3	0.27
47209.8	E- $^{13}\text{CH}_3\text{OH}$	47209.550	$1_{0,1}-0_{0,0}$	7.5	0.27
47249.3	E- $\text{CH}_3\text{OCOH } v_t=1$	47249.447	$4_{0,4}-3_{0,3}$	193.3	1.43
47277.1	U				
47293.7	$^{34}\text{SO}_2$	47293.169	$21_{2,20}-20_{3,17}$	218.6	0.12
47355.0	CH_2CHCN	47354.650	$5_{0,5}-4_{0,4}$	6.8	8.20
47374.7	AA- CH_3OCH_3	47374.428	$13_{3,10}-12_{4,9}$	95.8	1.05
47378.3	EE- CH_3OCH_3	47377.890	$13_{3,10}-12_{4,9}$	95.8	1.05
47381.5	AE- CH_3OCH_3	47381.058	$13_{3,10}-12_{4,9}$	95.8	1.05
	EA- CH_3OCH_3	47381.643	$13_{3,10}-12_{4,9}$	95.8	1.05
47420.4	CH_2CHCN	47419.796	$5_{2,4}-4_{2,3}$	15.5	6.92
47445.0	CH_2CHCN	47443.883	$5_{3,2}-4_{3,1}$	26.3	5.28
47549.6	U				
47462.4	OC^{34}S	47462.353	$J=4-3$	5.7	0.28
47490.2	CH_2CHCN	47489.231	$5_{2,3}-4_{2,2}$	15.5	6.95
47513.8	H86 ϵ	47511.871			
47534.3	E- CH_3OCOH	47534.116	$4_{0,4}-3_{0,3}$	5.2	1.46
47537.1	A- CH_3OCOH	47536.905	$4_{0,4}-3_{0,3}$	5.8	1.46
47557.0	p- CH_2OCH_2	47556.913	$5_{5,0}-5_{4,1}$	33.5	0.75
47603.2	H91 ζ	47601.583			
47658.9	U				
47661.0	SO_2	47660.621	$31_{5,27}-30_{6,24}$	519.0	0.26
47675.0	EA- CH_3OCH_3	47674.049	$1_{1,1}-0_{0,0}$	2.3	0.56
	AE- CH_3OCH_3	47674.066	$1_{1,1}-0_{0,0}$	2.3	0.56
	EE- CH_3OCH_3	47674.958	$1_{1,1}-0_{0,0}$	2.3	0.56
	AA- CH_3OCH_3	47675.858	$1_{1,1}-0_{0,0}$	2.3	0.56
47752.4	H73 γ	47749.977			
47766.4	H80 δ	47764.347			
47785.9	He80 δ	47783.813			
47793.7	AA- CH_3OCH_3	47793.664	$9_{1,9}-8_{2,6}$	40.9	0.07
47796.5	EE- CH_3OCH_3	47796.327	$9_{1,9}-8_{2,6}$	40.9	0.07
47810.4	H103 ι	47808.933			
47913.6	SO_2	47913.427	$14_{2,12}-13_{3,11}$	108.1	0.28
	H64 β	47914.182			
47927.2	HC_5N	47927.274	$J=18-17$	21.9	11.7
47935.6	He64 β	47933.707			
48001.7	$^{33}\text{SO}_2$	48002.505	$10_{3,7}-11_{2,10}$	72.3	0.25
48071.9	E- CH_3OCOH	48072.207	$18_{-4,14}-18_{4,15}$	113.8	0.10
48120.9	SO_2	48120.430	$21_{2,20}-20_{3,17}$	219.5	0.14
48155.4	H51 α	48153.597			
48175.0	He51 α	48173.219			
48178.8	C51 α	48177.620			
48206.7	C^{34}S	48206.942	$J=1-0$	2.3	1.67
48247.5	E- $\text{CH}_3\text{OH } v_t=1$	48247.571	$J_K=1_0-0_0$	302.9	0.35
48257.2	A- $\text{CH}_3\text{OH } v_t=1$	48257.310	$1_{0,1}-0_{0,1}$	426.0	0.35
48284.4	o- H_2CO	48284.513	$4_{1,3}-4_{1,4}$	32.7	0.36
48291.8	H95 η	48289.787			
	H99 θ	48290.070			
48372.4	A- CH_3OH	48372.460	$1_{0,1}-0_{0,1}$	2.3	0.36
48377.2	E- CH_3OH	48376.887	$J_K=1_0-0_0$	7.5	0.36
48496.0	O ^{13}CS	48495.061	$J=4-3$	5.8	0.30
48529.7	E- $^{13}\text{CH}_3\text{OH}$	48529.770	$7_{-2,6}-8_{-1,8}$	81.6	0.17
48553.3	CH_2CHCN	48552.564	$5_{1,4}-4_{1,3}$	9.2	8.49
48586.0	C^{33}S	48586.506	$J=1-0$	2.3	1.71
48589.0	EE- CH_3COCH_3	48588.915	$13_{7,6}-13_{6,7}$	72.6	3.09
48618.8	p- H_2CO	48617.998	$11_{2,9}-11_{2,10}$	279.7	0.21
48630.7	A- $\text{CH}_3\text{OCOH } v_t=1$	48630.383	$4_{3,2}-3_{3,1}$	200.2	0.69
48651.8	OCS	48651.604	$J=4-3$	5.8	0.30
48670.2	A- $\text{CH}_3\text{OCOH } v_t=1$	48669.924	$4_{3,1}-3_{3,0}$	200.2	0.69

Table 4: continued.

Observed Freq. (MHz)	Species	Rest Freq. (MHz)	Transition J_{K_a,K_c}	E_{upp} (K)	A_{ul} $\times 10^{-6} \text{ (s}^{-1}\text{)}$
48708.3	E-CH ₃ OH $v_t=1$	48708.074	$J_K=21_3-22_4$	950.7	0.58
48766.9	A-CH ₃ OCOH	48766.974	$4_{2,3}-3_{2,2}$	8.5	1.19
48768.4	E-CH ₃ OCOH	48768.254	$4_{2,3}-3_{2,2}$	7.9	1.19
48901.8	AE-CH ₃ OCH ₃	48900.278	$7_{1,6}-7_{0,7}$	27.6	0.68
	EA-CH ₃ OCH ₃	48900.278	$7_{1,6}-7_{0,7}$	27.6	0.68
	EE-CH ₃ OCH ₃	48901.416	$7_{1,6}-7_{0,7}$	27.6	0.68
	AA-CH ₃ OCH ₃	48902.554	$7_{1,6}-7_{0,7}$	27.6	0.68
48991.1	CS	48990.957	$J=1-0$	2.4	1.75
49001.3	o-CH ₂ OCH ₂	49000.973	$3_{2,2}-3_{1,3}$	11.8	0.73
	A-CH ₃ OCOH $v_t=1$	49000.801	$10_{2,8}-10_{1,9}$	224.4	0.22
49028.5	E-CH ₃ OCOH $v_t=1$	49028.893	$4_{2,3}-3_{2,2}$	196.0	1.20
49134.7	A-CH ₃ OCOH	49134.613	$4_{3,2}-3_{3,1}$	11.9	0.71
49151.5	E-CH ₃ OCOH	49151.621	$4_{3,2}-3_{3,1}$	11.3	0.70
49155.8	E-CH ₃ OCOH	49155.295	$4_{-3,1}-3_{-3,0}$	11.3	0.70
49158.2	H90 ζ	49155.858			
49163.1	H85 ϵ	49161.342			
49173.7	H102 ι	49171.605			
49180.0	A-CH ₃ OCOH	49180.088	$4_{3,1}-3_{3,0}$	11.9	0.72
49187.1	E-CH ₃ OCOH $v_t=1$	49186.907	$4_{2,2}-3_{2,1}$	196.3	1.22
49199.1	U				
49215.9	o-CH ₂ OCH ₂	49216.009	$8_{5,3}-8_{4,4}$	76.2	1.72
49461.9	AA-CH ₃ OCH ₃	49461.106	$4_{0,4}-3_{1,3}$	9.1	0.36
	EE-CH ₃ OCH ₃	49461.858	$4_{0,4}-3_{1,3}$	9.1	0.36
	AE-CH ₃ OCH ₃	49462.609	$4_{0,4}-3_{1,3}$	9.1	0.36
	EA-CH ₃ OCH ₃	49462.612	$4_{0,4}-3_{1,3}$	9.1	0.36
49509.3	A-CH ₃ OCOH $v_t=1$	49508.993	$4_{2,2}-3_{2,1}$	197.0	1.25
49533.1	o-CH ₂ OCH ₂	49533.149	$10_{7,3}-10_{6,4}$	118.2	1.98
49558.7	H79 δ	49556.792			
49729.3	H72 γ	49726.698			
49765.7	U				
49962.9	NH ₂ D	49962.831	$2_{1,2}-2_{0,2} \nu=0-1$	50.1	16.3

Notes. †: Observed frequency in red means that the line is below 3σ (see Fig. 6).

Table 6: Physical parameters derived by the models

Species	Component	v_{LSR} (km s ⁻¹)	Δv (km s ⁻¹)	d_{sou} ($''$)	T_K (K)	$n(H_2)$ (cm ⁻³)	N (cm ⁻²)	Method	Collisional rates
CS	Extended ridge	9.0	4.0	Extended	60	1×10^5	$(5 \pm 2) \times 10^{14}$	LVG	(a)
	Plateau	6.0	25	30	125	1×10^6	$(1.0 \pm 0.3) \times 10^{15}$	LVG	(a)
	Compact ridge	7.5	4.0	15	110	1×10^6	$(5 \pm 2) \times 10^{15}$	LVG	(a)
	Hot core	5.5	10	10	225		$(2.1 \pm 0.6) \times 10^{16}$	LTE	
C ³⁴ S	Extended ridge	9.0	4.0	Extended	60	1×10^5	$(1.0 \pm 0.3) \times 10^{13}$	LVG	(a)
	Plateau	6.0	25	30	125	1×10^6	$(8 \pm 2) \times 10^{13}$	LVG	(a)
	Compact ridge	7.5	4.0	15	110	1×10^6	$(8 \pm 2) \times 10^{13}$	LVG	(a)
	Hot core	5.5	10	10	225		$(7 \pm 2) \times 10^{14}$	LTE	
¹³ CS	Extended ridge	9.0	4.0	Extended	60	1×10^5	$(2.0 \pm 0.6) \times 10^{12}$	LVG	(a)
	Plateau	6.0	25	30	125	1×10^6	$(1.0 \pm 0.3) \times 10^{13}$	LVG	(a)
	Compact ridge	7.5	4.0	15	110	1×10^6	$(2.0 \pm 0.6) \times 10^{13}$	LVG	(a)
	Hot core	5.5	10	10	225		$(2.0 \pm 0.6) \times 10^{14}$	LTE	
C ³³ S	Extended ridge	9.0	4.0	Extended	60	1×10^5	$(1.0 \pm 0.3) \times 10^{12}$	LVG	(a)
	Plateau	6.0	25	30	125	1×10^6	$\leq (5.0 \pm 2.0) \times 10^{12}$	LVG	(a)
	Compact ridge	7.5	4.0	15	110	1×10^6	$\leq (1.0 \pm 0.3) \times 10^{13}$	LVG	(a)
	Hot core	5.5	10	10	225		$\leq (1.0 \pm 0.3) \times 10^{14}$	LTE	
CCS (upper limit)	Extended ridge	9.0	4.0	Extended	60	1×10^5	$(2.0 \pm 0.6) \times 10^{12}$	LVG	(b)
	Plateau	6.0	25	30	125	1×10^6	$(2.0 \pm 0.6) \times 10^{12}$	LVG	(b)
	Compact ridge	7.5	4.0	15	110	1×10^6	$(7 \pm 2) \times 10^{12}$	LVG	(b)
	Hot core	5.0	6.0	10	225		$(5 \pm 2) \times 10^{13}$	LTE	
CCCS	Extended ridge	10.0	4.0	Extended	60		$(4 \pm 1) \times 10^{12}$	LTE	
	Hot core	5.0	6.0	10	225		$(2.0 \pm 0.6) \times 10^{13}$	LTE	
HCS ⁺	Extended ridge	9.0	4.0	Extended	60	1×10^5	$(1.0 \pm 0.3) \times 10^{12}$	LVG	(c)
	Plateau	6.0	25	30	125	1×10^6	$(5 \pm 2) \times 10^{13}$	LVG	(c)
	Compact ridge	9.0	4.0	15	110	1×10^6	$(8 \pm 2) \times 10^{13}$	LVG	(c)
	Hot core	5.5	10	10	225		$(5 \pm 2) \times 10^{13}$	LTE	
OCS	Extended ridge	9.0	4.0	Extended	60	1×10^5	$(8 \pm 2) \times 10^{14}$	LVG	(d)
	Plateau	6.0	25	30	125	1×10^6	$(5 \pm 2) \times 10^{15}$	LVG	(d)
	Compact ridge	7.5	4.0	15	110	1×10^6	$(1.0 \pm 0.3) \times 10^{15}$	LVG	(d)
	Hot core	5.5	10	10	225		$(1.5 \pm 0.3) \times 10^{16}$	LTE	
OC ³⁴ S	Extended ridge	9.0	4.0	Extended	60	1×10^5	$(1.0 \pm 0.3) \times 10^{14}$	LVG	(d)
	Plateau	6.0	25	30	125	1×10^6	$(5 \pm 2) \times 10^{14}$	LVG	(d)
	Compact ridge	7.5	4.0	15	110	1×10^6	$(2.0 \pm 0.6) \times 10^{14}$	LVG	(d)
	Hot core	5.5	10	10	225		$(1.0 \pm 0.3) \times 10^{15}$	LTE	
O ¹³ CS (upper limit)	Extended ridge	9.0	4.0	Extended	60	1×10^5	$(3.0 \pm 0.9) \times 10^{13}$	LVG	(d)
	Plateau	6.0	25	30	125	1×10^6	$(1.0 \pm 0.3) \times 10^{14}$	LVG	(d)
	Compact ridge	7.5	4.0	15	110	1×10^6	$(2.0 \pm 0.6) \times 10^{14}$	LVG	(d)
	Hot core	5.5	10	10	225		$(9 \pm 3) \times 10^{14}$	LTE	
HC ₃ N	Extended ridge	9.0	4.0	Extended	60	1×10^5	$(4.0 \pm 1.0) \times 10^{13}$	LVG	(e)
	High velocity plateau	9.0	30	30	100	1×10^6	$(1.5 \pm 0.5) \times 10^{14}$	LVG	(e)
	Plateau	6.0	25	20	150	5×10^6	$(4 \pm 2) \times 10^{14}$	LVG	(e)
	Compact ridge	8.0	3.0	15	110	1×10^6	$(1.0 \pm 0.3) \times 10^{14}$	LVG	(e)
	Outer hot core	3.5	10	10	220		$(1.0 \pm 0.3) \times 10^{15}$	LTE	
	Inner hot core	5.5	7.0	7.0	310		$(6 \pm 2.0) \times 10^{14}$	LTE	
	20.5 km s ⁻¹ comp.	20.5	7.5	5	90	5×10^6	$(3 \pm 1.0) \times 10^{14}$	LVG	(e)
	Extended ridge	9.0	4.0	Extended	60	1×10^5	$(1.0 \pm 0.3) \times 10^{12}$	LVG	(e)
H ¹³ CCCN	High velocity plateau	9.0	25	30	100	1×10^6	$(2.0 \pm 0.6) \times 10^{12}$	LVG	(e)
	Plateau	6.0	25	20	150	5×10^6	$(1.0 \pm 0.3) \times 10^{13}$	LVG	(e)
	Compact ridge	8.0	3.0	15	110	1×10^6	$(8 \pm 2) \times 10^{12}$	LVG	(e)
	Outer hot core	3.5	10	10	220		$(2.0 \pm 0.6) \times 10^{13}$	LTE	
	Inner hot core	5.5	7.0	7.0	310		$(2.0 \pm 0.4) \times 10^{14}$	LTE	
	Extended ridge	9.0	4.0	Extended	60	1×10^5	$(5 \pm 2) \times 10^{11}$	LVG	(e)
	High velocity plateau	9.0	25	30	100	1×10^6	$(5 \pm 2) \times 10^{12}$	LVG	(e)
	Plateau	6.0	25	20	150	5×10^6	$(5 \pm 2) \times 10^{12}$	LVG	(e)
HC ¹³ CCN	Compact ridge	8.0	3.0	15	110	1×10^6	$(1.0 \pm 0.3) \times 10^{13}$	LVG	(e)
	Outer hot core	3.5	10	10	220		$(7 \pm 2) \times 10^{13}$	LTE	
	Inner hot core	5.5	7.0	7.0	310		$(1.2 \pm 0.3) \times 10^{14}$	LTE	
	Extended ridge	9.0	4.0	Extended	60	1×10^5	$(5 \pm 2) \times 10^{11}$	LVG	(e)
	High velocity plateau	9.0	25	30	100	1×10^6	$(5 \pm 2) \times 10^{12}$	LVG	(e)
	Plateau	6.0	25	20	150	5×10^6	$(5 \pm 2) \times 10^{12}$	LVG	(e)
	Compact ridge	8.0	3.0	15	110	1×10^6	$(1.0 \pm 0.3) \times 10^{13}$	LVG	(e)
	Outer hot core	3.5	10	10	220		$(7 \pm 2) \times 10^{13}$	LTE	
HCC ¹³ CN	Inner hot core	5.5	7.0	7.0	310		$(1.2 \pm 0.3) \times 10^{14}$	LTE	
	Extended ridge	9.0	4.0	Extended	60	1×10^5	$(5 \pm 2) \times 10^{11}$	LVG	(e)
	High velocity plateau	9.0	25	30	100	1×10^6	$(5 \pm 2) \times 10^{12}$	LVG	(e)
	Plateau	6.0	25	20	150	5×10^6	$(5 \pm 2) \times 10^{12}$	LVG	(e)
	Compact ridge	8.0	3.0	15	110	1×10^6	$(1.0 \pm 0.3) \times 10^{13}$	LVG	(e)
	Outer hot core	3.5	10	10	220		$(7 \pm 2) \times 10^{13}$	LTE	
	Inner hot core	5.5	7.0	7.0	310		$(1.2 \pm 0.3) \times 10^{14}$	LTE	
	Extended ridge	9.0	4.0	Extended	60	1×10^5	$(5 \pm 2) \times 10^{12}$	LTE	
HC ₃ N $v_7=1$	Plateau	6.0	25	20	150		$(2.0 \pm 0.6) \times 10^{14}$	LTE	
	Compact ridge	8.0	3.0	15	110		$(5 \pm 2) \times 10^{12}$	LTE	
	Outer hot core	3.5	10	10	220		$(8 \pm 3) \times 10^{14}$	LTE	
	Inner hot core	5.5	7.0	7.0	310		$(6 \pm 2) \times 10^{14}$	LTE	
HC ₃ N $v_6=1$	Extended ridge	9.0	4.0	Extended	60		$(1.5 \pm 0.3) \times 10^{12}$	LTE	
	Plateau	6.0	25	20	150		$(1.0 \pm 0.3) \times 10^{14}$	LTE	
	Compact ridge	8.0	3.0	15	110		$(8 \pm 3) \times 10^{12}$	LTE	
	Outer hot core	3.5	10	10	220		$(5 \pm 3) \times 10^{13}$	LTE	
	Inner hot core	5.5	7.0	7.0	310		$(3.0 \pm 0.9) \times 10^{14}$	LTE	
HC ₃ N $v_7=2$ (upper limit)	Extended ridge	9.0	4.0	Extended	60		$(1.0 \pm 0.3) \times 10^{12}$	LTE	
	Plateau	6.0	25	20	150		$(5 \pm 2) \times 10^{12}$	LTE	
	Compact ridge	8.0	3.0	15	110		$(1.0 \pm 0.3) \times 10^{12}$	LTE	
	Outer hot core	3.5	10	10	220		$(9 \pm 3) \times 10^{13}$	LTE	
	Inner hot core	5.5	7.0	7.0	310		$(2.0 \pm 0.6) \times 10^{14}$	LTE	
	Extended ridge	8.5	4.0	Extended	60	1×10^5	$(3.0 \pm 0.9) \times 10^{12}$	LVG	(f)

Table 6: continued.

Species	Component	v_{LSR} (km s ⁻¹)	Δv (km s ⁻¹)	d_{sou} ($''$)	T_{K} (K)	$n(\text{H}_2)$ (cm ⁻³)	N (cm ⁻²)	Method	Collisional rates
CH ₃ CH ₂ CN	Compact ridge	8.0	3.0	15	110	1×10 ⁶	(3.0±0.9)×10 ¹²	LVG	(f)
	Outer hot core	3.5	10	10	220		(7±2)×10 ¹³	LTE	
	Hot core 1	5.0	5.0	4	275		(6±2)×10 ¹⁶	LTE	
	Hot core 2	3.0	13	10	110		(4±1)×10 ¹⁵	LTE	
	Hot core 3	3.0	22	25	65		(1.5±0.3)×10 ¹⁵	LTE	
CH ₃ CH ₂ CN v_{13}/v_{21} (upper limit)	Hot core 1	5.0	5.0	4	275		(8±2)×10 ¹⁵	LTE	
	Hot core 2	3.0	13	10	110		(1.1±0.3)×10 ¹⁵	LTE	
	Hot core 3	3.0	22	25	65		(4±1)×10 ¹⁴	LTE	
CH ₂ CHCN	Hot narrow comp.	5.0	6.0	5	320		(3.0±0.9)×10 ¹⁵	LTE	
	Cold narrow comp.	5.0	6.0	10	100		(1.0±0.3)×10 ¹⁵	LTE	
	Hot wide comp.	3.0	20	5	200		(9±3)×10 ¹⁴	LTE	
	Cold wide comp.	3.0	20	10	90		(1.3±0.4)×10 ¹⁵	LTE	
NH ₂ CHO (upper limit)	Compact ridge	7.0	3.0	10	110		(7±2)×10 ¹⁴	LTE	
	Hot core	5.0	15	10	250		(6±2)×10 ¹⁴	LTE	
HNCO	Extended ridge	9.0	4.0	Extended	60		(5±2)×10 ¹³	LTE	
	Plateau	6.0	25	30	125		(5±2)×10 ¹⁴	LTE	
	Compact ridge	7.5	4.0	15	110		(5±2)×10 ¹⁴	LTE	
	Hot core	5.5	10	10	225		(7±2)×10 ¹⁴	LTE	
	Hot core (hot)	5.5	5.0	5.0	300		(5±2)×10 ¹⁵	LTE	
SO ₂	Extended ridge	8.5	4.0	Extended	60		(1.0±0.3)×10 ¹⁵	LTE	
	High velocity plateau	10	30	30	70		(1.6±0.5)×10 ¹⁷	LTE	
	Plateau	6.0	25	20	150		(1.4±0.4)×10 ¹⁶	LTE	
	Compact ridge	8.0	3.0	15	110		(1.2±0.4)×10 ¹⁶	LTE	
	Hot core	5.5	10	10	220		(2.3±0.7)×10 ¹⁷	LTE	
³⁴ SO ₂	20.5 km s ⁻¹ comp.	20.5	7.5	5	90		(8±2)×10 ¹⁴	LTE	
	Extended ridge	8.5	4.0	Extended	60		(1.0±0.3)×10 ¹⁴	LTE	
	High velocity plateau	11	30	30	100		(6±2)×10 ¹⁵	LTE	
	Plateau	6.0	25	20	125		(6±2)×10 ¹⁴	LTE	
	Compact ridge	8.0	3.0	15	110		(5±2)×10 ¹⁴	LTE	
³³ SO ₂ (upper limit)	Hot core	5.5	10	10	220		(1.0±0.3)×10 ¹⁶	LTE	
	20.5 km s ⁻¹ comp.	20.5	7.5	5	90		(4±1)×10 ¹³	LTE	
	Extended ridge	8.5	4.0	Extended	60		(3.5±1.0)×10 ¹³	LTE	
	High velocity plateau	11	30	30	100		(9±3)×10 ¹⁴	LTE	
	Plateau	6.0	25	20	125		(5±2)×10 ¹⁴	LTE	
¹³ CH ₃ OH ^(†)	Compact ridge	8.0	3.0	15	110		(7±2)×10 ¹³	LTE	
	Hot core	5.5	10	10	220		(3.5±1.0)×10 ¹⁵	LTE	
	20.5 km s ⁻¹ comp.	20.5	7.5	5	90		(8±3)×10 ¹²	LTE	
	Extended ridge	8.0	4.0	Extended	40		(4±1)×10 ¹⁴	LTE	
	Plateau	9.0	25	30	150		(6±2)×10 ¹⁴	LTE	
CH ₃ OH ^(†)	Compact ridge	7.5	4.0	15	110		(2.0±0.6)×10 ¹⁵	LTE	
	Hot core	5.5	10	10	250		(6±2)×10 ¹⁵	LTE	
	Hot core (hot)	7.5	4.0	7.0	300		(1.6±0.5)×10 ¹⁶	LTE	
	Extended ridge	8.0	4.0	Extended	40		(6±2)×10 ¹⁵	LTE	
	Plateau	9.0	25	30	150		(6±2)×10 ¹⁵	LTE	
A-CH ₃ OH $v_t=1$	Compact ridge	7.5	4.0	15	110		(1.0±0.3)×10 ¹⁶	LTE	
	Hot core	5.5	10	10	250		(6±2)×10 ¹⁶	LTE	
	Hot core (hot)	7.5	4.0	7.0	300		(1.6±0.5)×10 ¹⁷	LTE	
	Extended ridge	8.0	4.0	Extended	40		(2.5±0.7)×10 ¹⁴	LTE	
	Plateau	9.0	25	30	150		(3±1)×10 ¹⁴	LTE	
E-CH ₃ OH $v_t=1$	Compact ridge	7.5	4.0	15	110		(1.0±0.3)×10 ¹⁵	LTE	
	Hot core	5.5	10	10	250		(1.0±0.3)×10 ¹⁶	LTE	
	Hot core (hot)	7.5	4.0	7.0	300		(2.0±0.6)×10 ¹⁷	LTE	
	Extended ridge	8.0	4.0	Extended	40		(2.5±0.7)×10 ¹⁴	LTE	
	Plateau	9.0	25	30	150		(3±1)×10 ¹⁴	LTE	
o-H ₂ CO	Compact ridge	7.5	4.0	15	110		(1.0±0.3)×10 ¹⁵	LTE	
	Hot core	5.5	10	10	225		(3±1)×10 ¹⁵	LTE	
	Extended ridge	9.0	4.0	Extended	60		(1.0±0.3)×10 ¹⁵	LTE	
	Plateau	6.0	25	30	125		(2.0±0.6)×10 ¹⁵	LTE	
	Compact ridge	7.5	4.0	15	110		(3±1)×10 ¹⁵	LTE	
p-H ₂ CO	Hot core	5.5	10	10	225		(3±1)×10 ¹⁵	LTE	
	Extended ridge	9.0	4.0	Extended	60		(5±2)×10 ¹⁴	LTE	
	Plateau	6.0	25	30	125		(8±3)×10 ¹⁴	LTE	
	Compact ridge	7.5	4.0	15	110		(1.0±0.3)×10 ¹⁵	LTE	
	Hot core	5.5	10	10	225		(1.0±0.3)×10 ¹⁵	LTE	
o-H ₂ ¹³ CO (upper limit)	Extended ridge	9.0	4.0	Extended	60		(1.0±0.3)×10 ¹³	LTE	
	Plateau	6.0	25	30	125		(2.0±0.6)×10 ¹⁴	LTE	
	Compact ridge	7.5	4.0	15	110		(3±1)×10 ¹⁴	LTE	
	Hot core	5.5	10	10	225		(3±1)×10 ¹⁴	LTE	
	Extended ridge	8.0	4.0	Extended	60		(4±1)×10 ¹⁴	LTE	
CH ₃ OCOH ^(†)	Plateau	9.0	25	30	150		(1.6±0.5)×10 ¹⁵	LTE	
	Compact ridge	7.5	4.0	15	110		(1.4±0.4)×10 ¹⁶	LTE	
	Compact ridge (hot)	7.5	4.0	7.0	300		(4±1)×10 ¹⁶	LTE	
	Hot core	5.5	10	9.0	250		(8±3)×10 ¹⁵	LTE	
	Extended ridge	8.0	4.0	Extended	60		(4±1)×10 ¹³	LTE	
CH ₃ OCOH $v_t=1$ ^(†)	Plateau	9.0	25	30	150		(1.6±0.5)×10 ¹⁴	LTE	
	Compact ridge	7.5	4.0	15	110		(1.4±0.4)×10 ¹⁵	LTE	
	Compact ridge (hot)	7.5	4.0	7.0	300		(4±1)×10 ¹⁵	LTE	
	Hot core	5.5	10	9.0	250		(8±3)×10 ¹⁴	LTE	
	Hot core	5.5	10	9.0	250		(8±3)×10 ¹⁴	LTE	

Table 6: continued.

Species	Component	v_{LSR} (km s ⁻¹)	Δv (km s ⁻¹)	d_{sou} ($''$)	T_{K} (K)	$n(\text{H}_2)$ (cm ⁻³)	N (cm ⁻²)	Method	Collisional rates
CH ₃ OCH ₃ ^(††)	Plateau	9.0	25	30	150		$(8\pm3)\times10^{14}$	LTE	
	Compact ridge	7.5	4.0	15	170		$(7\pm3)\times10^{16}$	LTE	
	Compact ridge (hot)	7.5	4.0	7.0	300		$(2.5\pm0.7)\times10^{16}$	LTE	
	Hot core	5.5	10	9.0	250		$(4\pm1)\times10^{15}$	LTE	
NH ₂ D	Extended ridge	9.0	4.0	Extended	60		$(5\pm2)\times10^{13}$	LTE	
	Plateau	6.0	25	30	125		$(2.0\pm0.6)\times10^{14}$	LTE	
	Compact ridge	7.5	4.0	15	110		$(1.0\pm0.3)\times10^{14}$	LTE	
	Hot core	5.5	10	10	225		$(5\pm2)\times10^{14}$	LTE	
CH ₃ COCH ₃ ^(††) (upper limit)	Compact ridge	7.5	4.0	15	110		$(1.5\pm0.5)\times10^{15}$	LTE	
	Hot core	5.5	10	10	225		$(1.0\pm0.3)\times10^{15}$	LTE	
(o+p)-CH ₂ OCH ₂ (upper limit)	Extended ridge	9.0	4.0	Extended	40		$(3\pm1)\times10^{13}$	LTE	
	Compact ridge	7.5	4.0	15	110		$(7\pm3)\times10^{14}$	LTE	
CH ₃ NH ₂ (upper limit)	Extended ridge	9.0	4.0	Extended	60		$(8\pm3)\times10^{13}$	LTE	
	Plateau	6.0	25	30	125		$(8\pm3)\times10^{14}$	LTE	
	Compact ridge	7.5	4.0	15	110		$(8\pm3)\times10^{14}$	LTE	
	Hot core	5.5	10	10	225		$(5\pm2)\times10^{15}$	LTE	

Notes. (a): CS-He rates from ?; (b): Collisional rates derived from those of OCS (?) and from the IOS approximation for a ³Σ molecule (see ??); (c): HCS⁺-He rates from ?; (d): OCS-H₂ rates from ?. (e): HC₃N-p-H₂ rates from Wernli (2007). (f): HC₅N-H₂ rates estimate from the desexcitation rates of Deguchi & Uyemura (1984).

(†): A+E species; (††): AA+AE+EA+EE species.